The APEX-SZ Experiment: Observations of the Sunyaev Zel'dovich Effect

James Kennedy

Master of Science

Department

McGill University

Montreal,Quebec

2008-10-20

A thesis submitted to the Faculty of Graduate Studies and Research in partial fulfilment of the requirements for the degree of Master of Science

Your file Votre référence
ISBN: 978-0-494-67052-1
Our file Notre référence
ISBN: 978-0-494-67052-1

DEDICATION

This thesis is dedicated to my parents.

ACKNOWLEDGEMENTS

I thank my supervisor Matt Dobbs for his support and guidance throughout my Masters. I also thank everyone in the APEX-SZ collaboration, notably Adrian Lee, Nils Halverson, Amy Bender, Jared Mehl, Brad Johnson, Ben Westbrook, Cathy Horellou and Daniel Johansson for their support during APEX-SZ observations.

I would like thank everyone from my lab for making it an enjoyable environment to work in. I especially thank Trevor Lanting for his patience and guidance during the early stages of my Masters, Francois Aubin for the French translation of my abstract, and Kevin MacDermid for being a great lab mate.

Finally, I thank my parents, my brother, my sister, Audrey MacLeod, and all my friends for their never-ending encouragement in my work and life.

ABSTRACT

The Sunyaev Zel'dovich effect (SZE) is a secondary distortion of the cosmic microwave background (CMB) spectrum produced by galaxy clusters that allows for measurements of intra-cluster gas properties. Current experiments are using large arrays of multiplexed transition-edge sensor bolometers to achieve the sensitivities required for SZE cluster surveys and targeted cluster SZE observations. This thesis describes the APEX-SZ experiment, the first instrument to produce scientific results from observations with such an array. The scientific motivation for the APEX-SZ experiment is discussed, followed by a description of the APEX-SZ experiment and frequency domain multiplexing technologies. We have developed a custom data reduction pipeline for the experiment which uses a variety of filters, both in the temporal and spatial domain to produce 1' resolution maps of the SZE at 150GHz. The results of data analysis for the Bullet cluster (1E0657-56) and Abell 2204 (A2204) are presented. Both clusters are assumed to be isothermal and in hydrostatic equilibrium, allowing a fit to an isothermal β-model and subsequent mass fraction estimates. The maximum likelihood parameters and constant likelihood 68% confidence intervals are estimated using a Markov-Chain Monte Carlo method to sample the β-model parameter space. We measure cluster gas mass fractions with r_{2500} to be 0.140 ± 0.035 and 0.058 ± 0.035 for the Bullet cluster and A2204 respectively. The Bullet gas mass fraction is consistent with previous results from X-ray analysis. The gas mass fraction for A2204 does not agree well with other A2204 observations, however the large scatter in the gas mass fractions determined from previous X-ray and SZE analyses indicates that a more complex density model may be appropriate for this cluster.

ABRÉGÉ

L'effet Sunyaev Zel'dovich (SZE) produit une distorsion du spectre du rayonnement cosmologique fossile (CMB) permettant de mesurer les propriétés des amas de galaxies. Les expériences présentement en cours utilisent de grandes quantités de bolomètres en transition superconductrice multiplexés afin d'atteindre la sensibilité requise pour rechercher des amas de galaxies via l'effet SZE en plus d'étudier des amas connus. Ce mémoire décrit l'exprience APEX-SZ, le premier instrument à produire des résultats scientifiques à partir d'observations avec un tel plan focal de bolomètres. Les motivations scientifiques justifiant la pertinence de APEX-SZ sont discutées suivies de la description de l'expérience et de la technologie de multiplexage dans le domaine des fréquences. Nous avons développé une série de programmes d'analyse afin de réduire les données expressément pour cette expérience. Ces programmes utilisent une variété de filtres dans les domaines temporel et spatial afin de produire des mappe atteignant une résolution de 1' de SZE à 150GHz. Les résultats de l'analyse du "Bullet Cluster" (1E0657-56) et de Abell 2204 (A2204) sont présentés. Les hypothèses de l'isothermalité et de l'équilibre hydrostatique sont avancées pour ces deux amas, permettant l'ajustement du model bêta isothermal et subséquemment d'une estimation de la fraction de masse. La probabilité maximale des paramètres ainsi que la probabilité constante dans un intervalle de confiance à 68% sont estimées en utilisant la méthode en chane de Markov Monte Carlo afin d'échantillonner l'espace des paramètres du model bêta. Nous mesurons 0.140 ± 0.035 et 0.058 ± 0.035 pour la fraction de masse des amas à l'intérieur de r_{2500} pour le "Bullet Cluster" et A2204 respectivement. La valeur de fraction de masse du "Bullet Cluster" est cohérente avec les résultats précédent obtenus à partir des analyses de données rayons-X. La fraction de masse de A2204 diffère des autres observations. Cependant, le grand étendu de valeurs obtenues pour la fraction de masse de A2204 déterminée à partir d'analyses passées de données rayons-X et SZE indiquent qu'un modèle de densité plus complexe serait plus approprié pour A2204.

TABLE OF CONTENTS

LIST OF TABLES

LIST OF FIGURES

Figure | page

CHAPTER 1
Introduction

During the past decade, great advances have been made in cosmology. The developments have largely been driven by observations and experiments which, with increasing precision, have set limits on cosmic properties such as the fractional composition of baryonic matter, dark matter and dark energy. Observations of distant type 1a supernovae, large-scale galaxy surveys, measurements of cosmic abundances of the elements, and measurements of the cosmic microwave background (CMB) have all contributed to a concordance model of the universe and its evolution. As technology continues to advance, so do the opportunities and goals of experimental cosmology. Currently a new generation of experiments is using large arrays of multiplexed bolometers to measure the small-scale temperature anisotropies of the CMB. APEX-SZ is the first of these experiments. These CMB observations provide measurements of the properties of distant clusters of galaxies, which in turn constrain the universal cosmological parameters.

1.1 The Cosmic Microwave Background

Since its accidental discovery by Penzias and Wilson in 1964 [29], the CMB has been an exceptional probe of the early universe, allowing cosmology to become the precision science it is today. The CMB gives perhaps the strongest evidence for the Big Bang theory of cosmology, in which the universe has isotropically expanded from an initial singularity in space-time. During the early stages of its expansion, the universe was approximately in thermodynamic equilibrium. As the expansion and subsequent cooling continued, the temperature and density reached levels at which free electrons and protons could combine to form neutral atoms, making the universe transparent to radiation. This transition occurred at a redshift of $z = 1100$, which was about 400,000 years after the big-bang. The photons from this era, known as the surface of last scattering, are the CMB.

Following its discovery, experimentalists have attempted to measure the CMB frequency spectrum. In the early 1990's, the Far Infrared Absolute Spectrophotometer (FIRAS) experiment on the Cosmic Background Explorer (CMB) satellite made a high precision measurement providing substantial evidence for a blackbody spectrum at $2.726 \pm 0.010K$ [26]. This temperature is extremely uniform, indicating a highly isotropic early universe. However, small temperature anisotropies have been measured. The Differential Microwave Radiometer (DMR), flown on the COBE mission, measured the CMB temperature across the full sky with a resolution of $7°$ and found the anisotropy to be $\sim 10^{-5}$ [1].

Since COBE, a number of different CMB experiments have measured the CMB angular power spectrum, which characterizes the temperature fluctuations as a function of angular frequency, ℓ. Small angular frequencies, or low $\ell's$, correspond to large angular scales on the sky. The Wilkinson Microwave Anisotropy Probe (WMAP) satellite has measured the lower range of $\ell's$, providing the most sensitive measurements up to $\ell = 500$. The uncertainties in these measurements have reached their fundamental cosmic variance limit, which is the statistical uncertainty produced from having only one universe to sample from. Balloon-borne experiments such as MAXIMA and BOOMERANG, ground-based bolometer experiments such as ACBAR, and ground based interferometer experiments such as CBI and DASI, have measured the angular power spectrum to $\ell's$ of 3000 ($\sim 3'$). Additional measurements are needed at these $\ell's$ to reduce possible instrumental systematic errors, and measurements at higher $\ell's$ are required to set tighter constraints on cosmology.

Measurements of the primary temperature anisotropies, produced at the surface of last scattering, have provided estimates of the cosmological parameters such as the universal baryonic mass fraction and have indicated that the universe has a flat geometry. Anisotropies in the CMB produced after the surface of last scattering, known as secondary anisotropies, can provide information on structure in the universe at later times, detailing the evolution of structure formation.

1.2 Galaxy Clusters

The ΛCDM model, or concordance model of big-bang cosmology is the current leading theory of cosmology. It agrees with all current cosmological observations. This model describes the history of structure formation as developing from small-scale to large-scale. The seeds of structure were small density perturbations in the early universe, which grew through gravitational collapse into the first stars and galaxies. Gravity continued to drive these large-scale structures to further collapse, forming clusters of galaxies [36]. In this hierarchical picture, galaxy clusters form the largest and most recent virial objects in the universe. The masses of galaxy clusters can reach up to 10^{15} solar masses, producing gravitational potentials large enough to retain all their baryonic matter. The combination of their place in the structure formation chain and the retention of their baryonic components makes the study of galaxy clusters scientifically profitable as both a tracer for stellar and galactic evolution, and as a tracer for cosmology.

The masses of galaxy clusters are typically composed of $15-18\%$ baryonic matter, which itself is about 80% hot gas in the intracluster medium (ICM) and 20% stellar and galactic material [7]. The remaining cluster mass is made up of dark matter. The ICM contains mostly hydrogen and helium with traces of heavier elements. The temperature of the ICM, at 10^7-10^8K, is hot enough to ionize its constituents, creating free electrons and protons. The hot electrons in the ICM interact with both the passing CMB photons, as described in § 1.3, and other charged particles in the ICM. The deep potential wells within the ICM compress and heat the free particles producing X-ray emission dominated by thermal bremsstrahlung. The X-ray surface brightness is

$$S_X = \frac{1}{4\pi(1+z)^4}\int n_e n_i \Lambda_{ee} dl \tag{1.1}$$

where z is the cluster redshift, $n_{e,i}$ are the ICM electron and ion densities, Λ_{ee} is the X-ray emissivity, and the integral is taken along the line of sight.

X-ray flux observations of targeted galaxy clusters allow cluster temperature and density estimates. However, since $n_i \approx n_e$, the surface brightness is proportional the square of the electron density, making it sensitive to clumping in the ICM. Large angular scale X-ray emission surveys have been used to discover galaxy clusters. At low redshift, the ICM provides strong X-ray signals that stand out against the less dense intercluster medium. At redshifts above $z = 1$, the X-ray signal drops drastically and X-ray surveys quickly become inefficient for discovering clusters.

1.3 The Sunyaev Zel'dovich Effect

As mentioned in § 1.2, the hot electrons in the ICM can interact with CMB photons. These interactions, known as the Sunyaev Zel'dovich effect (SZE), are produced when a small fraction ($\sim 1\%$) of CMB photons passing through a galaxy cluster get inverse-Compton scattered off the ICM electrons. The resulting change in CMB photon energy will distort its blackbody spectrum. The angular size of the temperature anisotropy produced from the SZE is defined by the size of the cluster at the time of interaction and is typically on the order of an arcminute.

There are two general categories of the SZE: thermal and kinetic. The thermal SZE is produced by electrons whose motion is purely random thermal motion. Since the ICM electrons have a higher energy than CMB photons, on average the CMB photons will gain energy from the interaction, producing a characteristic distortion of the CMB frequency spectrum. The CMB blackbody spectrum and a simulated SZE spectrum are both shown in figure 1–1.

In the non-relativistic case, the SZE uniquely produces both a decrement in intensity below 217GHz and increment above this frequency. For cluster gas that is slightly relativistic, the frequency at which there is a null SZE signal varies slightly from 217GHz. The change in spectral intensity produced by the SZE is given by

$$\Delta I = I_{cmb} y g(x) \tag{1.2}$$

where $g(x) = \frac{x^4 e^x}{(e^x-1)^2}(x\frac{e^x+1}{e^x-1} - 4)[1 + \delta_{SZE}(x, T_e)]$ is the spectral form, δ_{SZE} is the relativistic correction, $x = \frac{h\nu}{kT}$ is the dimensionless frequency, and y is the Comptonization parameter.

$$y = \int (\frac{kT_e}{mc^2}) n_e \sigma_t dl \tag{1.3}$$

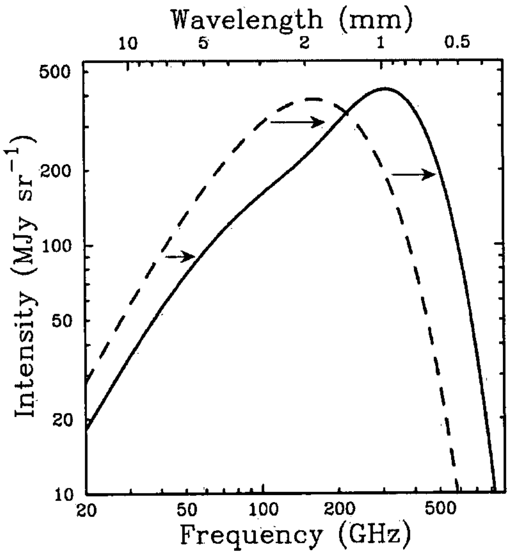

Figure 1–1: The CMB blackbody spectrum (dotted line) gets distorted by the inverse-Compton scattering of CMB photons with hot electrons in the intergalactic medium, producing the SZE spectrum (solid line). The simulated galaxy cluster is 1000 times more massive than an average cluster to emphasize the CMB spectral distortion. [4].

Here k is Boltzmann's constant, T_e is the electron temperature, n_e is the electron density, and σ_t is the Thompson cross-section and the integral is taken along the line of sight.

The corresponding temperature change of the CMB is given by

$$\Delta T = T_{cmb} y f(x) \tag{1.4}$$

where $f(x) = (x\frac{e^x+1}{e^x-1} - 4)[1 + \delta_{SZE}(x, T_e)]$ is the spectral form and T_{cmb} is the CMB temperature. Figure 1–2 shows both ΔI and ΔT for a range of electron temperatures and observing frequencies.

Another valuable property of the SZE, aside from its characteristic spectrum, is its redshift independence. The inverse-Compton scattering of CMB photons off hot electrons produces a fractional change in intensity and temperature through the cluster line of sight. The central SZE signal produced by a given cluster would be the same if that cluster were at any redshift. This property of the SZE makes it a powerful tool for the observation of the furtherest (and oldest) galaxy clusters.

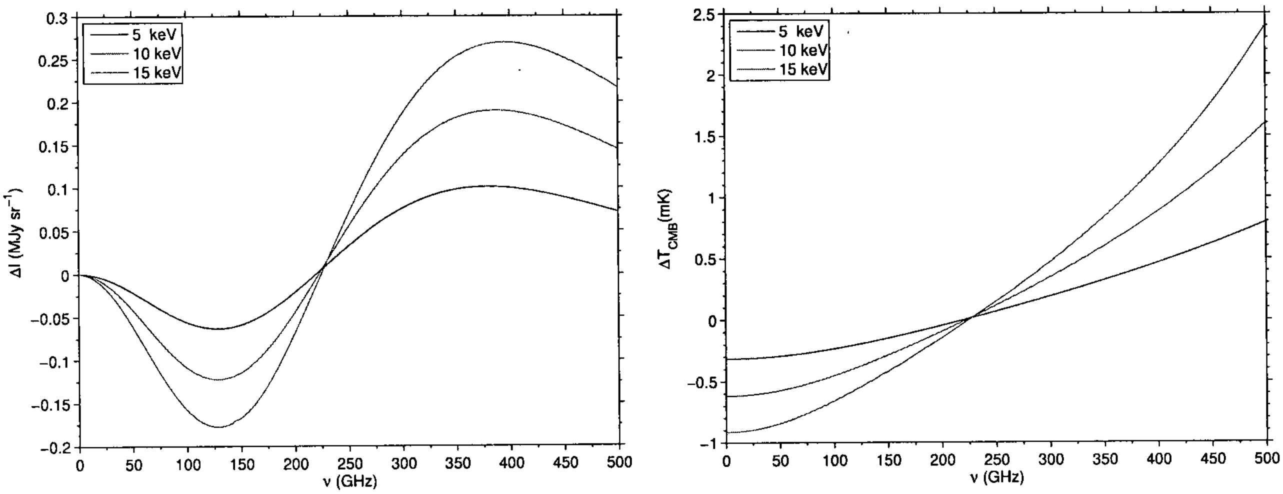

Figure 1–2: The SZE intensity and temperature spectral forms for cluster electron temperatures of 5, 10 and 15 keV. Left:The change in intensity as a function of frequency. Right: The change in temperature as a function of frequency. The simulated clusters all have the same electron density and line of sight depth.

The second category of SZE, known as kinetic SZE, is produced from the scattering of CMB photons off electrons in a cluster with a non-zero peculiar velocity in the CMB rest frame. In contrast to the thermal SZE, the kinetic SZE preserves the CMB blackbody spectrum, with only slight distortions in the relativistic case. In the non-relativistic case, the kinetic SZE produces a change in CMB temperature directly proportional to the peculiar velocity of the cluster. The signal from the kinetic SZE is expected to be much smaller than the thermal SZE for observations outside the thermal SZE null frequency range and no clear detection has yet been made.

1.4 The SZE and Cosmology

The SZE and X-ray emission from galaxy clusters provide complementary information about the ICM properties of the cluster. The SZE signal is $\propto n_e T$ whereas the X-ray signal is $\propto n_e^2 \Lambda_{ee}$, where Λ_{ee} is a complicated function of temperature. Observations of these two different physical processes can be combined to reveal the thermal and density structure of the cluster, which can then be used for cosmology. Since both the SZE and X-ray density integrals are taken over the line of sight, they can be used together to determine the distance to the cluster. Assuming that the distance through a cluster is proportional to the distance across the cluster, the line of sight integral is proportional to the angular diameter distance D_A. D_A is the distance to the cluster defined by its actual size and the angular size on the sky. The D_A of a cluster at a given redshift is dependent on the expansion of the universe, and hence the Hubble parameter. If the redshift of a cluster is known, the combined SZE and X-ray measurement of angular diameter distance provides a measurement of the Hubble parameter.

As stated in § 1.2, the baryon content in a galaxy cluster is believed to be unchanged since its formation. Due to the large size of the clusters it is assumed that the baryonic mass fraction, f_b, is a good approximation of the universal baryon fraction ($\frac{\Omega_B}{\Omega_M}$), where Ω_B is the universal baryon density and Ω_M is the universal mass density. Given an ICM electron temperature, the SZE provides a measurement of the cluster gas mass fraction, f_{gas}. The ICM constitutes the vast majority of the cluster baryon budget, so measurements of f_{gas} set a lower limit on $\frac{\Omega_B}{\Omega_M}$. If f_{gas} is measured for a range of redshifts, the normalization of the $f_{gas}(z)$ curve can place tight constraints on Ω_M and break the degeneracy between $\Omega_M(z)$ and the dark energy equation of state $w(z)$ [31].

Observations of galaxy clusters combined with their stellar baryon fraction have indicated that, on average, the cluster f_b values are smaller than the WMAP estimate of the universal baryon fraction by $\sim 10\%$ [9]. Many proposals have been made to account for the missing baryons in clusters. A variety of massive compact halo objects (MACHOs) could contribute to 'cold' baryons not observed in the X-ray or through the SZE, and difficult to detect in optical. However, reasonable estimates of both galactic MACHO species such as dwarf stars or planetary nebula, and cool intra-galactic baryons from dwarf galaxy tidal stripping and supernova contributions, are unlikely to completely account for the disagreement. Another possibility could be a the existence of a 'warm' ICM component ($\sim 10^5 - 10^7$K), maintained through the interaction between the ICM and the central active galaxy and/or thermal energy supplied from supernovae. This 'warm' ICM would provide a very weak bremsstrahlung and SZE signals [10]. Measurements of the SZE out to large radii can address this current problem by determining f_{gas} as a function of radius, and thereby reducing any measurement biases from local cluster effects such as core-cooling.

Another great strength of the SZE is its potential for cluster surveys. As discussed earlier, the magnitude of the central SZE signal does not change with redshift. Its total flux integrated over the cluster solid angle however, depends both on the magnitude of its signal and D_A^{-2}. The expected magnitude of the SZE signals from high redshift clusters and the small change in D_A at high redshifts allows a mass-limited SZE survey with little dependence on redshift above $z = 0.05$. This makes the SZE an excellent tool for the observation and discovery of clusters that are too far away for practical surveying in the visible and X-ray wavelengths. Once discovered, follow up observations in other wavelengths will provide redshift measurements to determine the cluster abundance evolution. The formation and abundance of clusters depends on the strengths of the local gravity and opposing forces, such as dark energy. Knowledge of the evolution of the cluster abundances as a function of mass and redshift will provide constraints on cosmology and $w(z)$.

1.5 SZE Experiments

SZE measurements fall into three main categories; single-dish radio measurements, interferometric radio measurements, and bolometeric measurements. The first SZE observations were made in the 1970s using general purpose telescopes to make single-dish radio measurements. These measurements used existing radiometric techniques, but lacked the ability (technological, logistical, or otherwise) to optimize their observations for SZE measurements.

Radio interferometry is another method for SZE observations. Large baselines used in interferometry can provide a high angular resolution unachievable in single dish telescopes, making interferometry a powerful tool for cluster ICM imaging. Also, when many telescopes and baselines are used, radio interferometry can separately observe large and small angular scales, aiding in point source removal and reducing radio confusion. However, due to the observation wavelength and telescope dish size, the telescope-baselines tend to lose signal at angular scales over several arcminutes. This reduces the ability of radio interferometers to be used for measurements of cluster f_g at large radii [2].

As will be discussed in § 2.1, bolometers have superior noise performance at higher frequencies when compared with radiometric devices. This allows SZE observations outside the Rayleigh-Jeans part of the CMB spectrum, giving a higher photon count and sensitivity. Also, bolometers can be arranged in arrays giving simultaneous measurements of different parts of the sky. This feature can be used to reduce atmospheric contributions (see chapter 4). Early measurements using bolometers were made by the Sunyaev-Zel'dovich Infrared Experiment (SuZIE). SuZIE used an array of six bolometers, each separated on the sky by ~ 2 arcminutes. As the array drift-scans across the sky, the bolometer signals were continuously differenced to measure the changes in sky brightness. The successful design led to a new generation of CMB experiments that use large arrays of multiplexed superconducting transition-edge sensor bolometers. The APEX-SZ experiment is the first of these new generation of experiments, and the topic of this thesis. The Atacama Cosmology Telescope (ACT) and the South Pole Telescope (SPT) are two of APEX-SZ's contemporary experiments, both achieving first light over a year after APEX-SZ. The APEX-SZ uses an array of 330 bolometer detectors, whereas SPT has an array of 960 detectors and ACT have 3072.

1.6 Thesis Outline

The outline for this thesis is as follows. In chapter 2, I will discuss the instrumentation used in APEX-SZ and other large array bolometer experiments. In chapter 3, I will focus on the specifics of the APEX-SZ experiment, from the telescope/optics to the readout system details. The observations and data analysis are described in chapter 4. Chapter 5 presents the analysis results for two galaxy clusters. Final conclusions are given in Chapter 6.

CHAPTER 2
CMB Instrumentation

Recent developments in technology have allowed for a new generation of CMB detectors and instrument readout systems that can achieve unprecedented detector array sensitivities. In this chapter we discuss the instrumentation used in the APEX-SZ and other current CMB experiments. Two main types of CMB detectors will be discussed, with a focus on transition-edge sensors. These detectors contain a superconducting temperature sensor, held in the transition between its normal and superconducting states by a voltage bias, and allow measurements of extremely slight variations in the CMB temperature. When each detector is biased at a different frequency, several of their signals can be added and amplified through one SQUID amplifier in a novel readout system known as frequency domain multiplexing. The TES bolometers and SQUID amplifiers require extremely low operating temperatures. I will discuss the design and operation of a liquid helium cryostat and three-stage sub-Kelvin ^3He Cooler absorption fridge used at McGill University. Together, the McGill cryostat and the ^3He absorption fridge achieves and maintains the cryogenic temperatures necessary to operate the TES bolometers and SQUID amplifiers. Our setup is used to measure the properties of bolometers and SQUIDs used in large format array CMB experiments such as APEX-SZ.

2.1 Detectors for CMB observations

Detectors of millimetre-wavelength radiation can measure photons signals either coherently or incoherently. Coherent detectors receive radiation using an antenna, which is typically coupled to a high electron mobility transistor (HEMT) amplifier [30]. The amplified signal can be mixed down to an intermediate frequency and measured directly. This method preserves the phase information of the incident radiation. However, at frequencies higher than 100GHz, coherent detectors reach their quantum noise limit due to the simultaneous photon position and frequency measurement uncertainty. Incoherent detectors measure the integrated power of the incident radiation and do not retain any phase information. Due to their superior noise performance above 100GHz, direct detectors are primarily used for CMB observations at high frequencies.

Bolometers are a common type of direct detector. Bolometers consist of an absorber with a heat capacity C, a temperature sensor and a temperature bath. The absorber is connected to the temperature bath through a heat link with a thermal conductance G. When the absorber is exposed to radiation with a power $P_{optical}$, its temperature rises above that of the temperature bath, increasing at a rate $dT/dt = P_{optical}/C$ to the maximum value $T = T_{bath} + P_{optical}/G$. The thermal time constant for the bolometer is $\tau = C/G$. The temperature sensor is thermally connected to the absorber and measures its change in temperature [32]. If the bolometer C, G, and T_{bath} properties are well known, the incident optical power can be inferred.

2.1.1 Transition-Edge Sensor Bolometers

Transition-edge sensor (TES) bolometers use a superconducting material, held in transition between its normal and superconducting states, as the temperature sensor. The sharp transition region of superconducting materials is characterized by $\alpha = d(logR)/d(logT)$ where R is the resistance of the sensor and T is its temperature. In this region, a small change in temperature produces a large change in resistance. TES bolometers have an α in the range of 50 to 500 [22]. During operation, the TES bolometers are voltage-biased, producing a change in current through the sensor for a change in sensor temperature. The voltage bias results in strong electrothermal feedback that holds the power on the bolometer constant since any change in optical power will result in a change in bolometer resistance, and thereby inversely change its electrical bias power, $P_e = V_b^2/R$ [25]. Figure 2–1 demonstrates this negative feedback system from a bolometer $I - V$ curve, in which V is the bias voltage and I is the current measured across the bolometer. A constant $P_{optical}$ is provided by a thermally radiating metal casing around the bolometer, kept at the same temperature as T_{bath}. At high voltages, the electric power drives the sensor into its normal state and the $I - V$ curve displays the constant slope expected from Ohm's law relation. As the voltage is decreased the sensor moves into its transition and its resistance decreases, producing an increase in electric power. The negative-electrothermal feedback loop provides us with an extremely sensitive, stable detector, whose current output is related to the incident sky power.

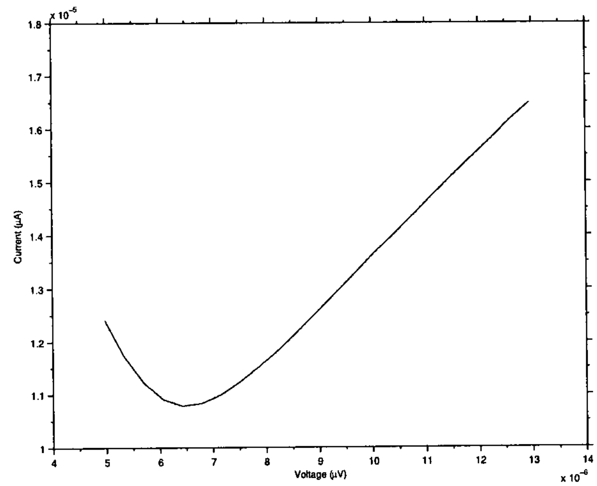

Figure 2–1: A bolo-iv curve for a South Pole Telescope (SPT) TES bolometer, measured in the McGill liquid helium cryostat. The curve displays the expected constant slope of Ohm's law at higher bias voltages. As the voltage is lowered, the TES drops into its transition, shown by the curve of constant power.

2.2 Frequency Domain Multiplexed Readouts of Bolometers

As individual bolometers reach their fundamental noise limit, due to the arrival statistics of individual photons, large arrays of detectors are implemented to increase sensitivity. APEX-SZ uses a frequency domain multiplexed (FDM) readout system to reduce the wiring complexity, cost of components, and heat-load on the cryogenic system that would be produced by individual detector readouts. In a TES bolometer FDM readout system, shown in figure 2–2, every detector is biased with a sinusoidal carrier voltage at a unique frequency selected using a resistor, inductor and capacitor circuit. The optical signal measured by the bolometer modulates the amplitude of the sinusoidal bias voltage, producing signal sidebands around the carrier in frequency space. The separation of detector signals in frequency space allows the output of several bolometers to be summed together and amplified by one SQUID amplifier. To reduce the required dynamical range of the FDM system, the carrier signal is nulled before its amplification through the SQUID. This is done by adding a sinusoidal signal to the bolometer output that is equal to the carrier signal, but has a phase shift of 90°. To accurately measure the FDM impedance and subsequent phase shift of the carrier signal, we omit a TES bolometer from the circuit and measure the output carrier signal. With the measured phase-shift, a nulling signal can be constructed an applied to the TES bolometer outputs.

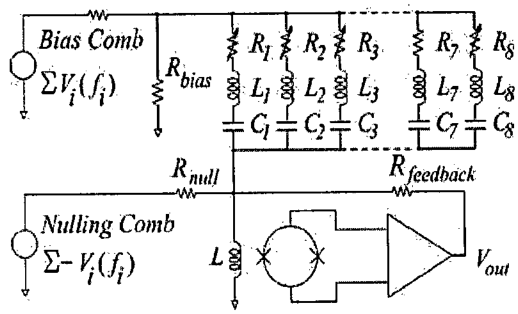

Figure 2–2: The schematic layout for a FDM bolometer readout system. Voltages at different frequencies are summed into a single bias frequency, resembling a comb in frequency space. The TES bolometers, indicated by the variable resistor symbols, use an inductor and capacitor as a tuned filter to select their unique bias frequencies. Finally, the signals from each bolometer are summed, the original carrier is cancelled using nulling comb, and the remaining signal is amplified using a SQUID amplifier.

2.3 SQUIDs

The SZE signal is expected to be extremely small, so low-noise electronics are necessary to observe a signal above the noise floor. We use a superconducting quantum interference device (SQUID) to amplify the bolometer signal before it leaves the cold cryostat environment for room temperature electronics. This device utilizes the Josephson junction, which is a thin insulating barrier linking two superconductors. The geometry of the Josephson junction allows the transmission of a super-current through the insulating barrier due to the quantum tunnelling effect [21]. The operation of SQUIDs also uses the phenomena of magnetic flux quantization in closed superconducting loop. For our SQUID amplifiers, two Josephson junctions are connected in parallel forming a closed loop as shown in figure 2–3. A constant current bias applied across the SQUID will be divided up between the two junctions, adhering to the quantization requirement that the total magnetic flux through the loop must be an integer multiple of the magnetic flux quanta $\Phi_0 = h/2e$. When the SQUID is exposed to an external magnetic flux, a circulating current will be induced in the loop to ensure that a flux of $n\Phi_o$ is maintained through the loop.

For a given constant current bias, a linearly increasing external magnetic flux will cause the SQUID voltage to oscillate between the maximum and minimum values needed to cancel the offset from $n\Phi$ [32]. The range between the minimum and maximum voltage values is governed by a number of factors, including the relative critical current between each Josephson junction, and any possible self inductance in the SQUID loop. $V - \Phi$ curves for several current biases are shown in figure 2–4. When kept in a flux-locked feedback loop, the voltage output of the SQUID can resolve deviations from Φ_o as small as $0.1\mu\Phi_o/\sqrt{Hz}$.

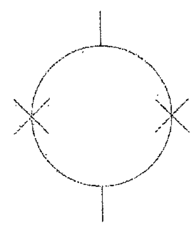

Figure 2–3: The schematic for a SQUID device. The circuit is composed of two Josephson junctions in parallel which form a closed superconducting loop. The crosses indicate a Josephson junction. [22]

A current biased SQUID can act as an ammeter and measure the currents from FDM TES bolometers. The current, summed from many bolometers, is carried along a line which coils adjacent to the SQUID, forming an inductor. The magnetic flux from this inductor is converted to a voltage by the induced current in the SQUID. This voltage can be sent from the cold electronics to the warm laboratory.

2.4 Cryogenics

The cold electronics in the frequency multiplexing system have to be powered, controlled, and read out from a room temperature laboratory environment. We have commissioned a liquid helium cryostat at McGill University to contain and isolate the various cold components from the room temperature laboratory and to control the flow of heat within. Although the APEX-SZ

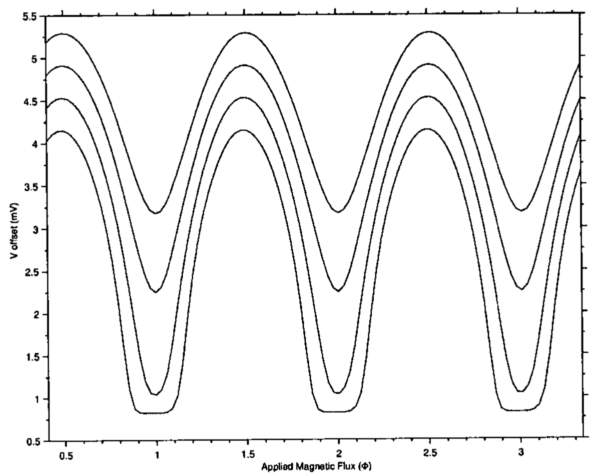

Figure 2–4: Four SQUID $V - \Phi$ curves, measured in the McGill liquid helium cryostat. Each curve has a different current bias across the SQUID. When an external magnetic field with a value of $n\Phi$ is applied to the SQUID, the induced voltage across the loop is a minimum. When there is an external magnetic flux with a value of $n\Phi/2$ the induced voltage across the loop, required to satisfy the magnetic flux quantization, is a maximum. The overall structure of the induced voltage is roughly sinusoidal.

experiment uses a pulse-tube cooler system to achieve a base temperature of 4 K and not liquid helium, our McGill cryostat acts as a test setup allowing us to test and measure the properties of cold TES bolometers and SQUID amplifiers for use in CMB experiments such as APEX-SZ. The cryostat achieves a base temperature of 4.2 K (boiling point of liquid helium at 1ATM) and brings the SQUIDs below their superconducting transition temperature. The main plate of a Simon Chase helium-10 absorption fridge is thermally connected to the 4.2 K cold plate of the cryostat and further reduces the temperature of the TES bolometers to 250 mK.

2.4.1 LHe Cryostat

The McGill liquid He cryostat, shown in figure 2–5, consists of three cylindrical shells, each at a different temperature during operation. The outside shell, also known as the 300 Kelvin shell is exposed to the laboratory room temperature. The inner shells are cooled to 77 Kelvin and 4.2 Kelvin using liquid nitrogen and liquid helium respectively. The cryostat is designed to maximize the time at which the inside shell can remain at 4.2 Kelvin.

Heat transfer from the warm laboratory and between the shells is possible through convection, conduction and radiation. Heat transfer through convection is drastically reduced by

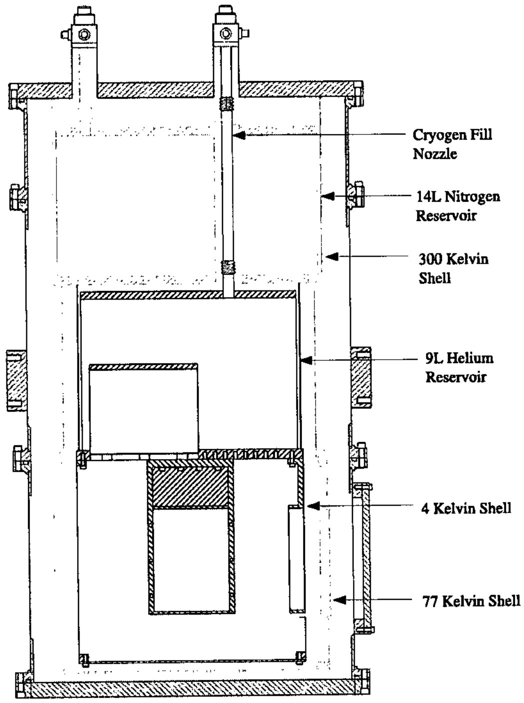

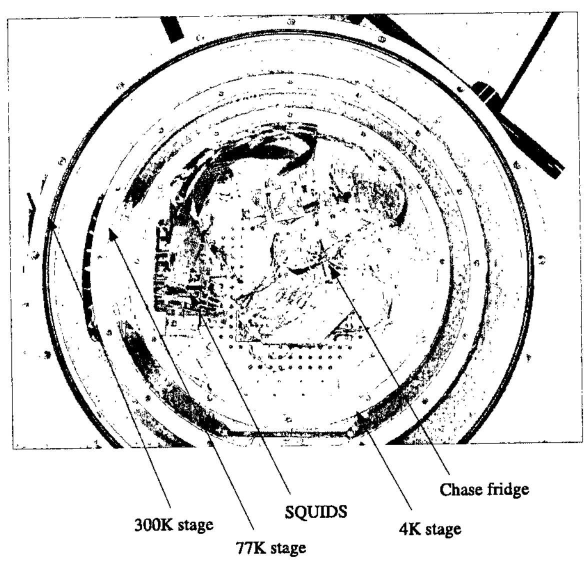

Figure 2–5: Images of the McGill liquid helium cryostat. TOP: A cross-sectional schematic of the cryostat showing the three shells, liquid reservoirs, fill nozzles and support structures. Adapted from the original manufacturer drawings by Mohamed Najih. BOTTOM: A photograph of inside the bottom of the cryostat. The three shells are visible, as with the absorption fridge heads (two brass circles), a gold plated bolometer wedge support structure, and three SQUID boards shielded in cyroperm.

pumping down the cryostat to high vacuum pressures. We use a turbo pump in combination with a roughing pump to achieve pressures on the order of 10^{-5} Torr. Once liquid cryogens are introduced, the remaining water and oxygen particles in the cryostat freeze to the 77 Kelvin and 4.2 Kelvin walls upon contact. Any remaining nitrogen particles will freeze to the 4.2 Kelvin wall, reducing the pressure to the order of 10^{-7} Torr.

The cost of liquid helium is much greater than liquid nitrogen, so the power from the 77 Kelvin shell to the 4.2 Kelvin shell must be known and minimized. The rate of conductive heat transfer through the cryostat by the shell supports, cryogen fill nozzles, and readout wires is given by

$$\dot{Q} = \frac{A}{\ell} \int_{T_1}^{T_2} \lambda(T) dT \tag{2.1}$$

where A is the cross-sectional area of the material, $\lambda(T)$ is its temperature-dependant thermal conductivity and ℓ is the length over which heat is being transfered between two bodies of temperature T_1 and T_2 [38]. To reduce $\dot{Q}$ we use a long thin cylinder of fibreglass for the support structure and a long thin cylinder of stainless steel for the fill nozzle. These materials achieve a balance of providing a strong structure while having a reasonably low thermal conductivity. Together they introduce heat to the 4 Kelvin shell at a rate of $0.16W$. There are a total of 160 manganin wires coming into the cryostat from 300 Kelvin stage. The are thermally connected to the 77 Kelvin stage before continuing to the 4 Kelvin stage. These wires connect the SQUID, TES bolometer and thermometry to the electronics outside the cryostat. The manganin wire provides good electrical conductivity while maintaining a low thermal conductivity at operating temperatures. The wires introduce heat at a total rate of $0.01W$. The thermal conductivities of cryostat materials connecting the 4 Kelvin stage to the 77 Kelvin stage are given in table 2–1. All the non-negligible forms of heat flow on the 4 Kelvin stage are given in table 2–2 with their power values.

Radiative heat transfer between the shells dumps a power of

$$\dot{Q} = \sigma A (T_1^4 - T_2^4) \frac{\varepsilon}{2 - \varepsilon} \tag{2.2}$$

Table 2–1: Mean Thermal Conductivity in $W/(cm \cdot K)$ for Cryostat Materials [38]

Material	Thermal Conductivity	Temperature Range
Stainless Steel	4.5×10^{-2}	77 - 4 K
Fibreglass	5.0×10^{-4}	77 - 4 K
Manganin	1.13×10^{-3}	77 - 4 K

Table 2–2: Heat flow into the 4 Kelvin Stage

Structure	Method	Power
Fill Nozzle	Conductive	$0.11W$
Fibreglass Supports	Conductive	$0.05W$
Manganin Wires	Conductive	$0.01W$
77 Kelvin Stage	Radiative	$0.02W$

Where σ is the Stefan-Boltzmann constant, A is the area of the 4 K shell, T_1 and T_2 are the temperatures of the 77 K and 4 K shell respectively, and ε is the emissivity of the shell material. The radiative power applied to the 4 K stage from the 77 K is $0.02W$. With the above power considerations, under no extra heat load, the liquid helium dewar's 9 litre storage tank can maintain 4 Kelvin temperature for up to 1.7 days. During typical operation, the power introduced by the absorption fridge cycles reduce this time to the order of a day.

2.4.2 He-10 Absorption Fridge

The boiling liquid helium can bring the temperature of the cryostat cold plate to 4.2 K. At this temperature the SQUIDS are in their superconducting regime, however the TES bolometers are well above their transition temperature of 550 mK. To achieve sub-Kelvin temperatures we use a three-stage sub-kelvin ^3He cooler, commonly known as a Chase helium-10 fridge, designed by Simon Chase. This fridge contains three helium reservoirs, one containing the helium-4 isotope, and two containing the helium-3 isotope[1] . A figurative schematic is shown in figure 2–6. Inside the same vacuum vessel, above the liquid helium, is a lining of charcoal, which is thermally connected to the 4 K cold plate through a gas cap switch. The liquid helium-4 in the reservoir absorbs heat from the interhead and boils into a gas. This gas is then absorbed by the charcoal

[1] The 4 and two 3's from the helium isotopes make up the 10 in the helium-10 fridge

lining. This reduces the pressure inside the reservoir, which reduces the boiling temperature of the helium-4. The helium-4 and helium-3 reservoirs are both contained in the interhead, forming an excellent thermal connection between them. The interhead itself is thermally connected to a separate helium-3 reservoir in the ultra-cold head through a mechanical heat link. When the boiling helium-4 reaches a low enough temperature the helium-3 samples can condense into a liquid and the above process is repeated. The pumping action by the charcoal lining in each reservoir reduces the boiling temperature of their respective cryogen. The interhead contains a large sample of helium-3 which is designed to act as an intermediate stage between the 4 Kelvin cryostat components and the ultracold head, and has a cooling power of 60 μW. Under a typical heat load, the interhead reaches temperatures around 350 mK. The ultra-cold head is exposed to this effective temperature of $350mK$ and is free to use all of its 1.5 μW of cooling power to bring the TES bolometers below their transition temperature. Under a typical heat load, the ultra-cold head can reach temperatures of $250mK$.

Once all of the liquid cryogens have been boiled off, the charcoal lining is heated to release the absorbed gas. When the helium-4 gas comes in contact with the 4.2 K stage, it condenses back into a liquid. After all the helium has boiled off the charcoal, the gas cap switches are closed, cooling the charcoal. The cool charcoal can then commence pumping, and the cycle is repeated.

With an operational liquid helium dewar at McGill University, we have measured detector and SQUID amplifier properties as can been seen in figures 2–4 and 2–1. These devices, when used in a FDM readout system like in the APEX-SZ experiment and other large format bolometer array experiments, are able to make extremely low noise and sensitive observations of the CMB. The resulting observations produce scientifically valuable measurements of the SZE and enable tight constraints to be placed on cosmological parameters.

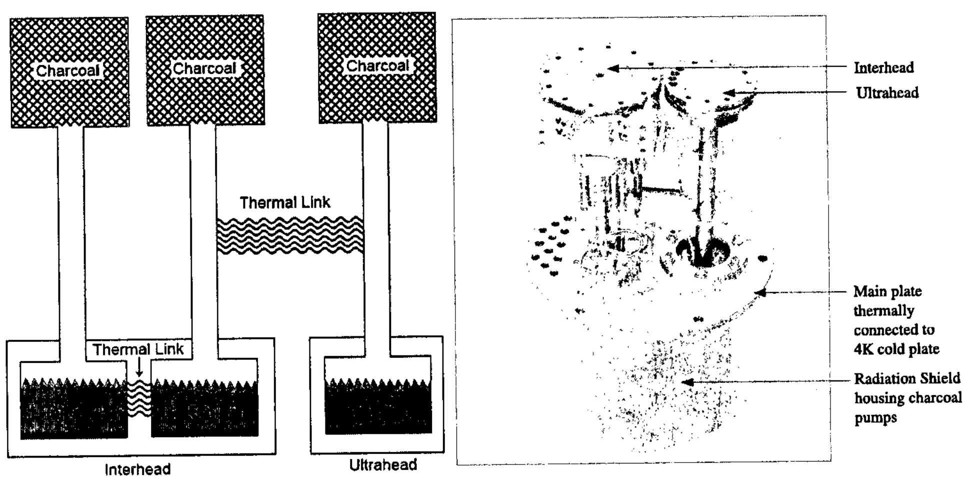

Figure 2–6: Left: A schematic of each helium reservoir and their relation to each other. This image was made by Mohamed Najih. Right: A photograph of McGill's Chase helium-10 fridge. The same type of fridge is used in the APEX-SZ experiment and other CMB experiments. [6]

CHAPTER 3
The APEX-SZ Experiment

The APEX Sunyaev Zel'dovich (APEX-SZ) experiment is an international collaboration between McGill University, the University of California, the University of Colorado, the Max Planck Institute for Radio Astronomy (MPIfR), Cardiff University in the UK, Chalmers University of Technology in Sweden, and the University of Bonn in Germany. It uses the APEX telescope to observe the SZE signal in the CMB. The secondary optics design achieves a diffraction limited 22' field of view, while sharing the instrument cabin with a number of facility instruments. The APEX-SZ receiver uses a 320-element array of TES bolometers cooled to 250 mK without expending cryogens. The detector signal is amplified using SQUID devices in an multiplexed readout system. Along with the telescope itself, the APEX-SZ experiment has been a pathfinder, demonstrating with scientific results the capabilities of the technology described in chapter 2. An APEX-SZ instrument summary is given in table 3–1

Table 3–1: APEX-SZ Summary Table

Primary Reflector	$12m$
Field of View	0.4°
Number of Active Detectors	280
Mean Beam Size	58"
Median Individual Pixel Noise Equivalent Power (NEP)	$10^{-16}W$
Median Individual Pixel Noise Equivalent Temperature (NET)	$1mK_{CMB}\sqrt{s}$

3.1 The APEX telescope

The Atacama Pathfinder EXperiment (APEX) telescope, shown in figure 3–1, is a $12m$ on-axis cassegrain telescope. It has been commissioned by the Max Planck Institute for Radio Astronomy (MPIfR), the European Southern Observatory (ESO) and the Swedish Onsala Space Observatory as a prototype antenna for the Atacama Large Millimeter Array (ALMA). It is located at an elevation of $5100m$ on the Atacama Plateau in Northern Chile, near other CMB

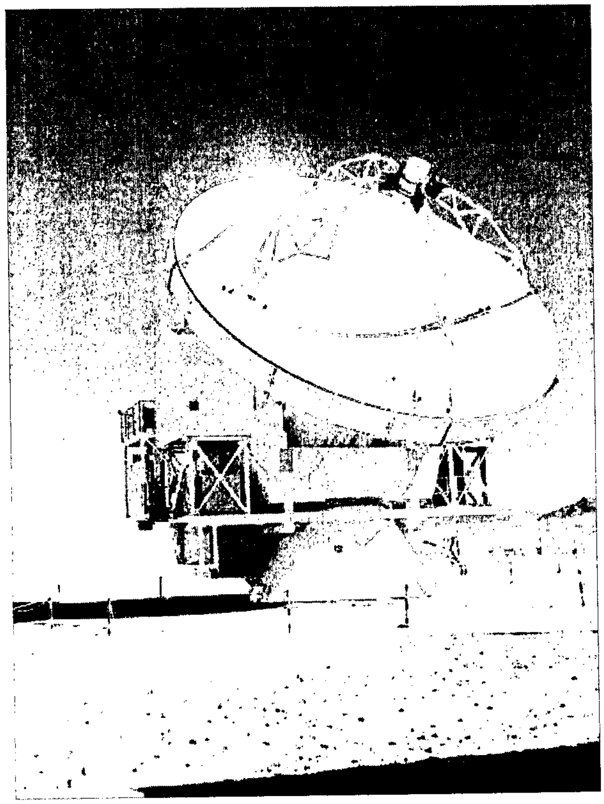

Figure 3–1: The APEX telescope on the Atacama plateau in Chile.

experiments such as the Atacama Cosmology Telescope (ACT), and the Cosmic Background Imager (CBI). The APEX telescope is a facility instrument for a number of single-dish submillimetre bolometer and heterodyne receivers. As such, the rms surface accuracy of $17-18\mu m$ [16], necessary for the submillimetre instruments, is more than acceptable for SZE observations of galaxy clusters.

The APEX site is one of the world's best locations for CMB observations due to its stable and extremely dry atmospheric conditions. Figure 3–2 shows the atmospheric transmission at the telescope for typical precipitable water vapour levels. APEX-SZ observes in a 23GHz band centred at 150GHz. The latitude of the APEX telescope, at 23°S, provides good overlap with patches of sky previously observed by other telescopes and satellite experiments, allowing for comparison with other wavelength observations.

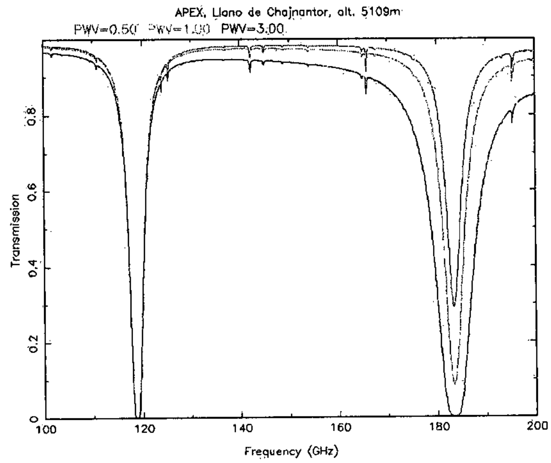

Figure 3–2: The zenith transmittance for various precipitable water vapour levels, calculated using an atmospheric transmission model developed at the Instituto de Estructura de la Materia Department of Molecular and Infrared Astrophysics. The transmission at the APEX-SZ centre frequency is rarely below 0.9. This image was produced at http://www.apex-telescope.org/sites/chajnantor/atmosphere/.

3.2 Optics

The APEX-SZ optics use three shared APEX telescope mirrors and two APEX-SZ specific mirrors. The $12m$ telescope primary reflects the sky signal to a $0.75m$ secondary hyperboloidal mirror held near the primary focal point with four carbon fibre reinforced plastic legs. The secondary mirror reflects radiation through a hole in the centre of the primary into the instrument cabin. There, the APEX tertiary mirror reflects incoming radiation to the APEX-SZ parabolic mirror, which in turn reflects to the APEX-SZ ellipsoidal mirror and finally into the receiver. The APEX-SZ ellipsoidal mirror forms a $10cm$ aperture image at a 4 K Lyot stop, which truncates diffractional spillover from the previous optics. An illustration of the optical system from inside the receiver cabin is shown in figure 3–3. Conical feedhorns and two 4 K lenses, housed in the cryostat after the Lyot stop, couple the light to the focal plane, achieving a $22'$ diffraction limited field of view [34].

The detector beam shapes are measured using raster scans of planetary sources, such as Mars and Jupiter. These planets appear as bright point sources at 150GHz. The mean measured full-width at half-maximum (FWHM) of the Gaussian beams is 58". The beam sizes across the array are shown in the right panel of figure 3–4. Using Fourier transform spectroscopy (FTS), we have measured our optical bandwidth to be $23GHz$ centred on $150GHz$ [27].

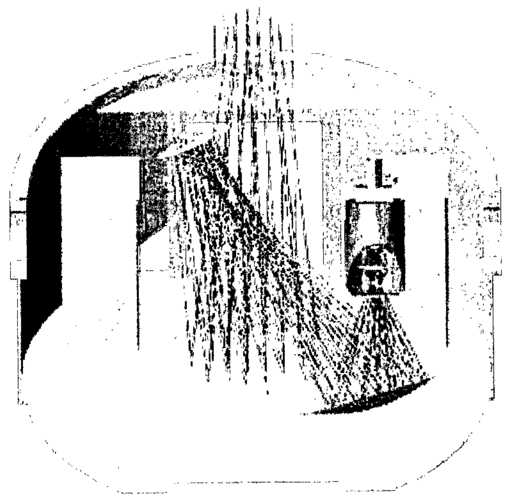

Figure 3–3: The APEX-SZ tertiary optics. Light enters the receiver cabin through a hole in the primary dish (not shown). It is then reflected off two parabolic mirrors to an ellipsoidal mirror below the APEX-SZ receiver. [34]

3.3 Receiver

The APEX-SZ receiver main plate is cooled to 4 K using an alternative method than the McGill liquid helium dewar described in § 2.4. The 4 K base temperature in the cryostat is achieved using a cryomech PT410 pulse tube cooler (PTC). This device more than doubles the cool down time from 300 K, however it contains all its cryogens in a closed system. This reduces the cost of operation, and the logistical complications of transporting a supply of liquid helium to the APEX site. From the 4 K base temperature a Chase helium-10 fridge, identical to the one described in § 2.4, is used to cool the bolometer array to 290 mK.

The focal plane houses an array of 6 bolometer wedges with each wedge containing 55 TES bolometer detectors, shown in the left panel of figure 3–4. The TES detectors have been monolithically fabricated to provide uniformity across each wedge. The bolometer absorber is constructed from gold traces, arranged in a spiderweb mesh that is $3mm$ in diameter. The spiderweb mesh geometry provides a low cross-section for cosmic rays, while maintaining high cross-section for millimetre wavelength radiation. The optical time constant for the bolometers is determined by the thermalization time of the spiderweb absorber and is measured to be $\sim 9ms$. The temperature sensor of the bolometer is constructed from a bilayer of aluminium and titanium, shown in figure 3–5. The titanium has been added to aluminium to reduce its superconducting temperature (T_c) through the proximity effect. The thickness of the aluminium and titanium layers are adjusted to give a TES T_c of 550 mK [22]. A 3 μm gold ring is thermally connected to the TES to increase its heat capacity and reduce the electrical time constant of the system, allowing the TES to remain stable when it is within its superconducting transition region [27]. The average thermal conductance for these spiderweb TES bolometers is $\bar{G} \simeq 250pW/K$

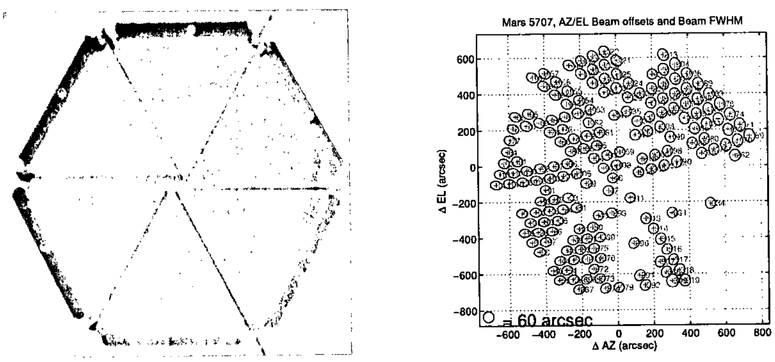

Figure 3–4: Left: A photograph of the APEX-SZ TES bolometer array [27]. Right: The measured APEX-SZ bolometer array beams from the Mars raster scan 5656, taken on April 6 2007.

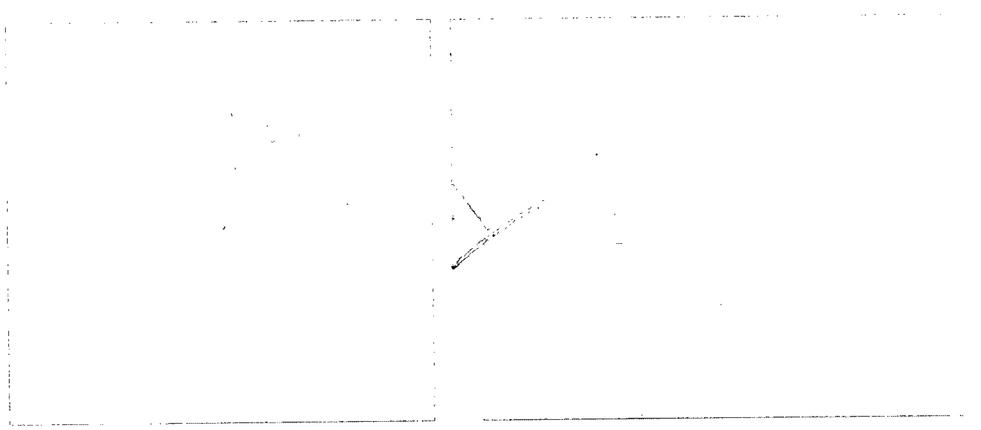

Figure 3–5: Left:An individual spiderweb TES bolometer. Right: A close of up this spiderweb's transition-edge sensor and gold ring. [8]

The APEX-SZ frequency domain multiplexing (FDM) readout system biases the detectors with an AC comb of frequencies from 200 kHz to 1 MHz, reading out 7 bolometer detectors with one SQUID amplifier. The omission of some TES bolometers, allowing a measurement of the carrier voltage phase shift as described in § 2.2, reduces the number of active detectors from 330 to 280. With the remaining channels, we measure a median detector noise-equivalent power of $100aW/\sqrt{Hz}$ and a median noise-equivalent temperature of $1000\mu K_{cmb}\sqrt{s}$. An example bolometer noise spectrum is shown in figure 3–6. The data, recorded during the December 2005 engineering run, were taken with the receiver window closed and the telescope in motion to replicate the conditions of a typical science observation. The noise spectrum includes contributions from readout electronics, Johnson noise, SQUID noise, and bolometer noise. The smooth curve is the predicted value, and the dotted curve is the noise spectrum for a channel with no bolometer, indicating the noise contribution from the SQUID and readout alone.

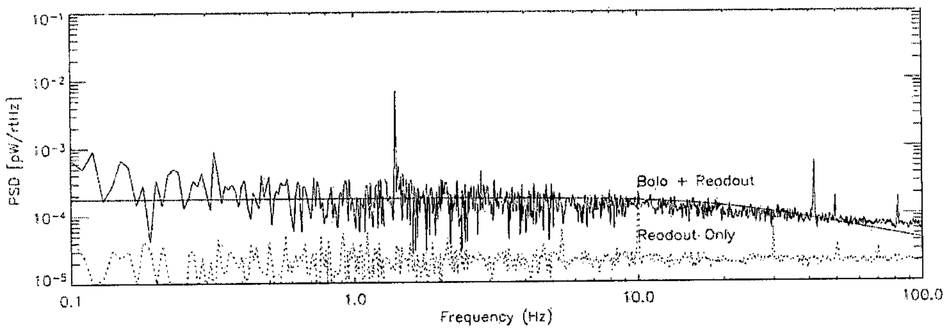

Figure 3–6: Measured noise spectrum for a bolometer readout channel(solid line) and a readout channel with no bolometer(dotted line). The smooth curve indicates the theoretical prediction of the bolometer readout noise. The large spike at 1.4Hz is produced by the operation of the PTC and is easily removed by filtering. [8]

The APEX-SZ experiment, mounted on the APEX telescope, was first deployed in December of 2005 for an engineering run for instrument characterization. Since that time it has been used for 4 separate science observation runs, with a 5^{th} planned for November 2008. I have worked with the APEX-SZ collaboration to develop a custom data reduction pipeline for analysis of the APEX-SZ science data. The data reduction procedure is described in chapter 4.

CHAPTER 4
Observations

The main goal of targeted galaxy cluster observations with the APEX-SZ experiment is a sky map at 150 GHz which most resembles the true sky. This chapter discusses the observational considerations required to produce the final sky map, from the observation strategy, to data processing, calibration and map-making as outlined in figure 4–1. We first explore the different telescope scanning strategies employed by the APEX-SZ experiment in § 4.1. The resulting measured signal includes instrumental effects from the telescope optics and readout, foregrounds such as atmospheric signal, and the SZE signal imposed on the CMB. We have developed a pipeline to reduce the contamination from atmospheric emission and correlated noise signals. The motivation and procedure for each filter is discussed in § 4.2. In § 4.3 we outline the methods of direct calibration, using an astronomical source with a known flux at 150 GHz, and indirect calibration, using astronomical sources with a stable flux, and opacity corrections. Finally, in § 4.4 we describe the 2 dimensional binning of data to produce the final sky map.

4.1 Scan Strategies

One feature of the APEX-SZ experiment that makes it a powerful tool for scientific observations is its large array of detectors. The array allows for 280 separate observations of sky signal to be made simultaneously, providing high sensitivity. The main goal of the scanning strategy is to maximize the time each detector points at the target and to modulate the sky signal above the $1/f$ noise in the timestreams. The signal from our target however, is buried under dominating foreground signals from elevation dependant airmass signal due to the atmospheric column density, large scale atmospheric signal variations due to weather turbulence, and potential ground pickup. The most appropriate scanning strategy will exploit the properties of these foregrounds to separate them from the cluster signal.

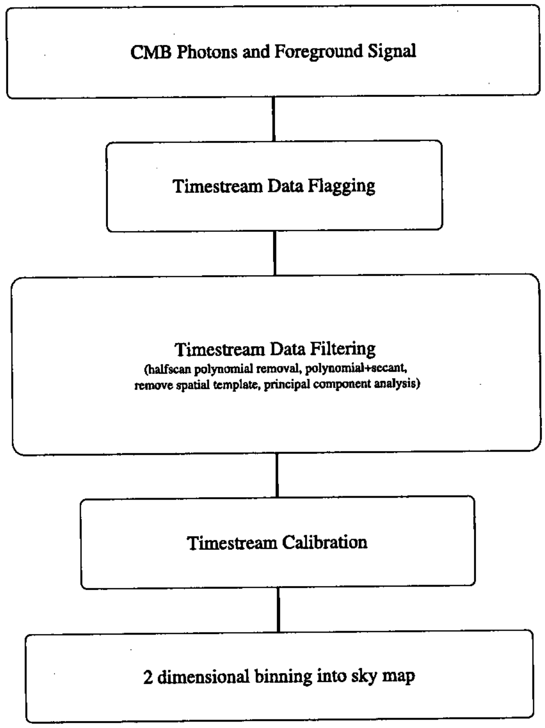

Figure 4–1: A flowchart illustrating the general procedure for producing a sky map from CMB photons.

The raster scan pattern, shown in figure 4–2, swings the telescope dish in the azimuth direction while holding the telescope elevation constant. When a full swing of the telescope, called a halfscan,[1] is completed the telescope makes a step in the elevation direction and repeats the pattern many times to produce a full scan. The raster scan pattern for our cluster observations uses a 4'/s swing in the azimuth direction, making a 0.5 degree sky trace centred on the target cluster. In between halfscans there is a step in elevation, the length of which depends on the new position of the source, but is typically around 0.25'. Since there is no change in elevation during a single halfscan, each detector will see a constant atmospheric airmass signal appearing in the timestream as a constant baseline. An unfortunate consequence of the raster scan is the large amount of time incurred during the telescope turn-arounds in between halfscans. The

[1] A single halfscan does not constitute one half of the full scan. The unfortunate name comes from historical nomenclature.

high telescope acceleration during the turn-around periods can cause mechanical vibrations in the telescope and readout. The vibrations reduce the accuracy of the pointing data and can introduce noise into the data. Also, the small telescope velocity during the turn around times allows a significant change in atmospheric foreground with poor modulation in the desired signal. Due to its low quality, data taken during this time is removed. The raster scan pattern was originally designed for large-area sky surveys, in which the telescope make large swings in the azimuth direction. For small-area targeted cluster observations, the turn around times are comparable to the small swing in azimuth. After removing the turn around periods we are left with slightly more than 50% of the original data. During our August 2007 observing run, our science goals focused on pointed cluster observations as opposed to large-scale cluster surveys. To increase the on-sky observing efficiency for the smaller area scanning fields used in pointed cluster observations, we developed a circular drift scan pattern and reduced the use of the raster scan.

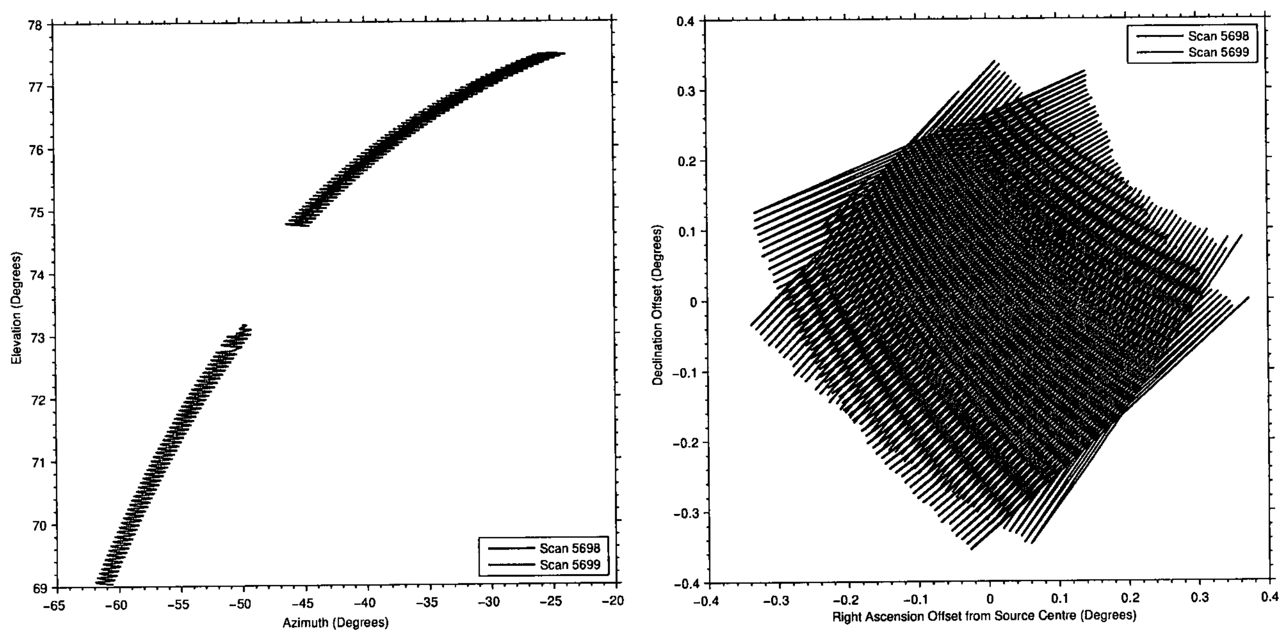

Figure 4–2: The pattern on the sky produced from raster scan 5698 of the galaxy cluster RXCJ1347-1144. Left: The telescope azimuthal and elevation offsets from source centre. Right: The corresponding absolute right ascension and declination sky traces.

Our circular drift scan pattern, illustrated in figure 4–3, traces a number of circles on the sky, centred on constant telescope azimuth and elevation coordinates, while the target cluster drifts through the telescope field of view. We defined a halfscan as one complete circle and a unit scan set as all the circles centred on a telescope azimuth and elevation coordinates. We typically chose a circle radius of 6' and period of 5 seconds to reduce any significant change in the atmosphere during a single halfscan. The acceleration of the telescope during the circle scans is much more moderate than the accelerations incurred during the raster scan turn-arounds and we do not see any vibrational effects on the bolometers. However, during the May 2005 observing run, we found that our bolometer temperatures would slightly increase during a scan due to the effects of vibrations on our Chase helium-10 fridge. To reduce the vibrations produced during the telescope rotation, we changed our circle radius from 6' to 8' thereby increasing the period of the circles.

The change in elevation made during a single scan introduces a large signal from changing atmospheric column depth, but it is modulated to the scan circle frequency. By removing any high acceleration periods, such as the raster scan turn-arounds, the drift circle scan pattern reduces the amount of data cut from a scan. The circle pattern of the first halfscan in a circle set tends to deviate from the rest of the halfscans as it moves from the telescope stationary position into the drift circle motion, and is typically cut. Roughly 20% of observation time was spent moving the telescope to the next circle scan position before the next unit scan set, making the circular drift scan pattern a more efficient scan strategy for targeted clusters than the raster scan.

4.2 Timestream Filtering

The 280 raw detector timestreams from each scan are sampled at 100Hz and combined with the detector biasing and configuration data, the cryogenic thermometry data, the telescope timing and pointing data interpolated to the same rate as the detector data, and are written to disk. Initial cuts are made on the data to remove periods of poor quality, due to the scanning strategies described in § 4.1, then any remaining periods of low quality data are flagged and removed from the subsequent data processing stages as described in § 4.2.1. The good data must then be filtered for correlated, atmospheric signals before they can be binned into sky maps.

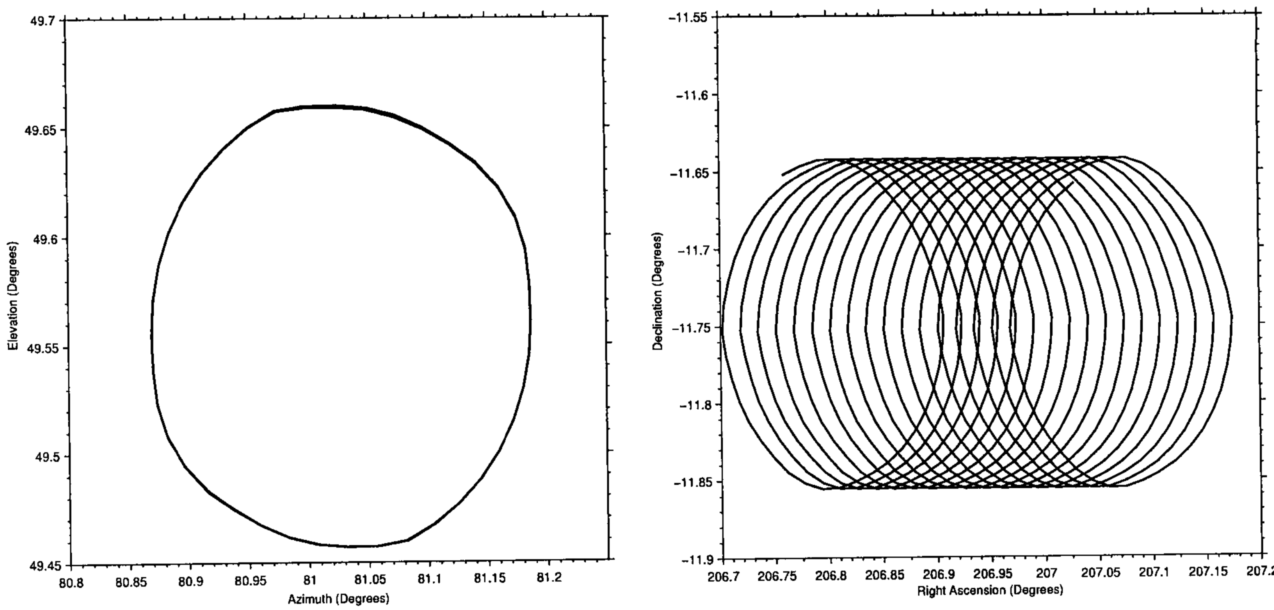

Figure 4–3: The sky pattern produced from circle drift scan 32649 of the galaxy cluster RXCJ1347-1144. Left: The telescope azimuthal and elevation offsets from source centre. Right: The corresponding absolute right ascension and declination sky traces.

4.2.1 Data Cuts and Flagging

The telescope pointing data are used to first parse the raw timestream data into halfscan and unit scan sets before any flagging and filtering is applied. For raster scans, regions of constant velocity are found and indexed as halfscans. The turn around regions, indicated by the gaps in these constant velocity regions, are cut from the data. In the case of the drift circles, the velocity vector in the azimuth direction forms a sinusoidal curve over the full scan. Individual halfscans are identified and indexed as one cycle of this sinusoidal curve, starting from zero velocity in the positive direction. Individual unit sets are identified by large changes in the mean telescope position of each halfscan. If there was any erratic telescope motion during a scan, the halfscan and unit scan set identifier algorithms would fail and incorrectly parse the scan into the wrong sections. Also, this would introduce atmospheric column-depth signal in a way that is difficult to identify and remove. To reduce the possibility of these errors we cut any halfscans which are not within 20% of the mean halfscan length. We then cut any unitscan sets that are not within 40% of maximum unit scan set length.

The remaining low quality data are then flagged, preventing their involvement in subsequent filtering and sky map binning. First, the full detector channel flags are applied, removing their data from any lengthy processing. The channels with an optical efficiency below 8% are flagged, where the optical efficiency is defined as the ratio of change in electrical power on the detector to the change in incident optical power. This typically leaves between 160-180 good detectors. The optical efficiency of each channel is calculated using the closest calibration scan, which has a known incident optical power. Channels are also flagged if they exceed their dynamical range limits during a scan. When this occurs, the raw adc counts of the timestream "rail" to a value of ± 7000 and no further change in signal can be measured.

The next step in the data filtering is to flag glitches from the individual timestreams. The origins of the glitches are not well understood, but some could be attributed to cosmic ray hits in the detector or electromagnetic interference from an external source. They appear in the data as sharp spikes that occur on timescales faster than our detector optical time constant. Since our target clusters have a signal-to-noise ratio of < 1 in a single timestream, we can identify glitches as any signal that exceeds a 6σ deviation from the mean signal in a halfscan, after a first-order polynomial is removed. Next, the power-spectral-density for each detector channel is measured and channels with excessively high or low noise in the signal band averaged between 12Hz and 18Hz are flagged. Since glitches and noise can be correlated across many detector channels, we have a final flag cut routine which sets a threshold on the maximum percentage of flags that can occur during a halfscan before the whole halfscan itself is flagged. We repeat this process for a threshold of flags per time step, channel, and unit scan set. We typically run this routine after flagging glitches and again after flagging noisy channels, using thresholds of $100\%, 100\%, 0.1\%, 100\%$, and $50\%, 25\%, 100\%$, and 50% respectively.

4.2.2 Atmospheric Subtraction

After the flagging of low-quality data, we apply filters that reduce the atmospheric signals in our timestreams. The location of the APEX site and the observing frequency band of the experiment were chosen to minimize the effect of atmospheric signals on our data. Even so, it remains the dominant signal in our timestreams. The water vapour contained in the atmosphere has a strong dipole moment with rotational transitions that lead to emission in the millimetre wavelengths. The resulting opacity of the atmosphere produces a large-scale signal from the line of sight airmass, and noise from small-scale fluctuations in the column depth of the water vapour.

To first order, the airmass signal can be modelled by assuming a homogeneous plane-parallel atmosphere. Ignoring the curvature of the Earth, optical path length through the airmass is proportional to the cosecant of the elevation angle. The plane-parallel assumption is valid for elevation angles above 30°, the minimum observation angle for the APEX telescope. The turbulence in the atmosphere introduces noise into our timestreams superimposed on the airmass baseline. Atmospheric turbulence is produced by convection, wind shear and gravity forces acting on large scales of atmosphere. The large-scale turbulence is dissipated to smaller scales through eddy flows until its length scale is $\sim 1mm$, producing a power spectrum that is well described by the Kolmogorov model. Using this model the atmospheric turbulence signal can be described as a static sheet of atmosphere blowing across the telescope field of view at some wind speed [24]. The emission from the atmospheric airmass and the Kolmogorov turbulence are both highly correlated across the 0.4° field of view of the APEX-SZ array, whereas the SZE signal from clusters, which are typically on arcminute scales, is not. We have used three major filtering methods to reduce the effect from the atmosphere; principal component analysis (PCA) and a spatial template removal, which exploit the high correlation of atmospheric signals separate it from the target cluster signal, and a polynomial+secant function removal which uses the elevation dependence of the airmass signal. Each filter is described in detail below.

Principal Component Analysis

PCA is used by many fields in science and statistics to find correlations between multi-dimensional data. The APEX-SZ PCA reduction finds correlations between detectors, where each detector is treated as a single dimension. First, the mean of each timestream is removed so that relative, and not absolute signals will be compared between detectors. Then the covariance matrix is calculated, which determines the level of correlations between detectors across the array.

We use the eigenvectors of the covariance matrix to provide us with a basis in correlation space, where the highest correlation across the array will produce the eigenvector with the largest eigenvalue, known as the principal component. The signal producing the highest correlation across the array can be isolated by projecting the timestream data onto the principal component eigenvector. This projection, along with other high order projections, can be removed from the timestreams, leaving the uncorrelated noise and cluster signals.

The PCA reduction removes a significant amount of large-scale correlated signal, as shown in figure 4–4, however, the reduction filter has notable flaws. A large fraction of data is needed at each timestep to calculate the proper covariances between detectors. This condition requires us to flag entire time steps if only a few are bad quality, and results in an unacceptable amount of data loss. A second unappealing issue with PCA is its reduction basis. Since the reduction takes place in correlation space, it is difficult to understand and quantify the non-linear transfer function for the filter and account for any loss of cluster signal. We have detected a significant amount of signal loss when using PCA reduction on our scans of the Bullet cluster. Due to this, we developed lighter filters that have better-understood transfer functions.

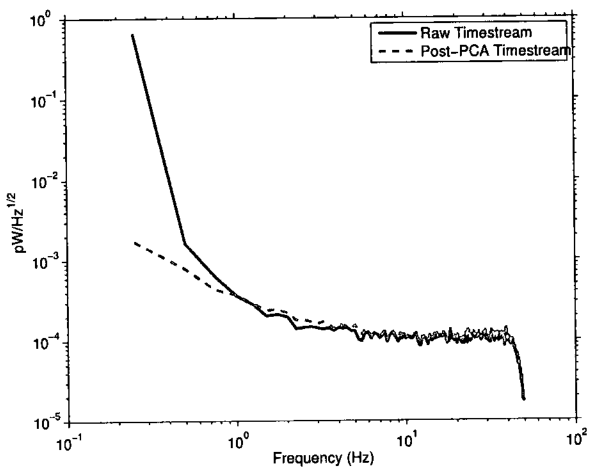

Figure 4–4: The power spectral density (PSD) of the timestream for detector 102 during a targeted cluster observation. The solid blue-line is the PSD of the raw timestream data. The dashed red-line is the PSD of the timestream after PCA filtering has been applied. Large-scale signals appear as $1/f$ in a data timestream due to the scanning of the telescope.

Spatial Template Removal

We have implemented a spatial template filter similar to that used in other CMB experiments such as Bolocam [33]. Much like PCA, this filter uses the fact that the atmosphere signal will be correlated across the bolometer array. Unlike PCA, the spatial template removal works in the spatial domain with no time evolution information. At each time-step a plane, tilted plane, or parabolic-tilted plane is fitted across all the unflagged bolometer channels and removed. For proper implementation, the relative gains of the channels are measured before any template fitting. We use a flat-field method which uses a reference signal to compare with the channels across the array. The reference channel is constructed from the median signal across all unflagged detectors at each time-step. For each detector, at each time-step, we take the ratio of the channel signal to the reference signal. The median ratio is the channel's relative flat-field gain. This filter can remove highly correlated signals detected across our detector array and its transfer function is well understood. Also, since it works time-step by time-step, it can be applied to both the raster scans and drift circle scans and is typically used in all our reductions.

Polynomial-Secant removal

Since the drift circle scan strategy has become the primary scan pattern for APEX-SZ observations, we have designed a polynomial-secant removal function which utilizes the modulation of the sky to identify and reduce the atmospheric airmass signal. The polynomial-secant removal filter simultaneously fits a secant and a high order polynomial across a full unit scan set. The secant component removes the airmass signal, and the polynomial function will fit to any baseline drifts over the unit scan set. We typically match the order of the polynomial to the number of halfscans contained in the unit scan set. The potential mixing between the polynomial function and the secant has been tested by fitting a high order polynomial to a pure secant and measuring the residual signal. Any degeneracy between the functions is negligible for 20^{th} order polynomials and less.

The polynomial+secant filter has provided excellent removal of any baseline drifts and atmospheric airmass signal when they are the dominating noise. The polynomial+secant is less effective when the atmospheric turbulence is high causing the signal-to-noise of the atmospheric airmass secant to be reduced. Nevertheless, the polynomial+secant provides a quantifiable transfer function and, in combination with the spatial template removal, is a standard filter for circular drift scans.

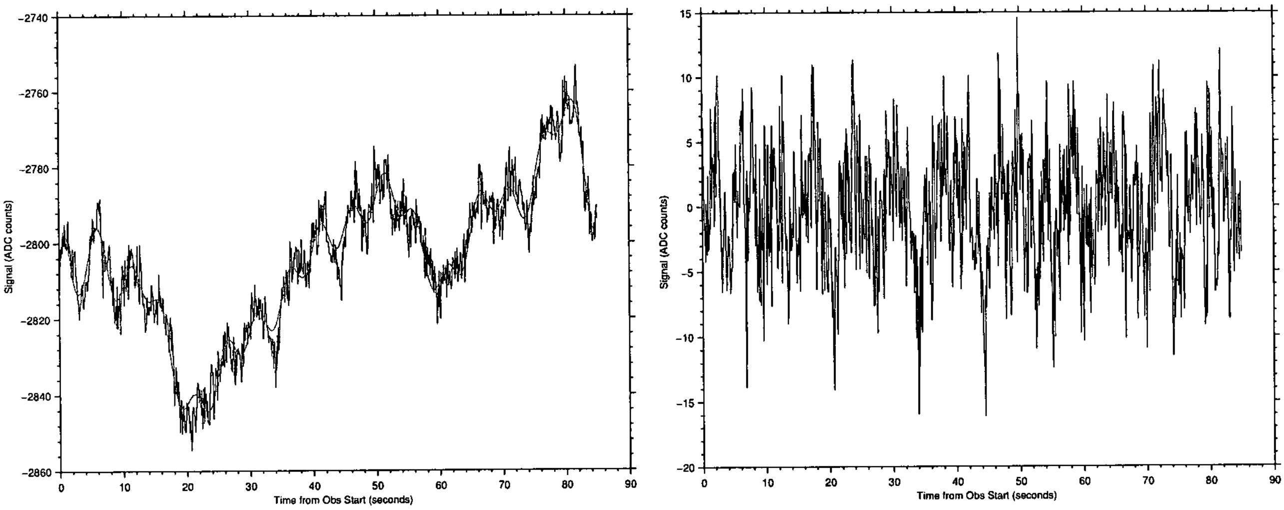

Figure 4–5: The effect of polynomial+secant removal on a circle drift scan of the Bullet Cluster. Left: The timestream before any polynomial+secant removal. Only typical flagging has been performed. The jagged line is the timestream data and the smooth line is the polynomial+secant fit. Right: The timestream after the polynomial+secant fit has been removed.

4.3 Calibration

A timestream is a record of the signal detected by an individual beam, stored in analog-to-digital (ADC) counts. An accurate determination of the beam properties, and temperature calibration is necessary for a reconstruction of the sky signal in meaningful units, such as Kelvin. To measure our beams and calibrate the detectors, the APEX-SZ experiment makes daily scans of a bright astronomical source with a well measured flux profile.

For the primary flux and beam shape calibrations, we make raster scans of Mars. The resulting timestream is a convolution of the Mars and detector beam profiles. The radius of Mars is typically between 1.5" and 8", less than 15% of our beam full-width at half-maximum (FWHM), so we can treat it as a delta function profile in the convolution, allowing a measurement of our beam shapes to 1% uncertainty. Before any convolution process occurs, we first remove a 1^{st} order polynomial from each detector timestream. We then make individual channel maps and fit a 2-dimensional Gaussian, centred on the maximum calibrator signal. The best-fit Gaussian amplitude, FWHM values in orthogonal directions, and direction of ellipticity provide the necessary parameters to characterize the shape of our beams. The telescope pointing has been referenced to one specific detector on the array. Combining the telescope pointing, which has been referenced to a single channel on the array, with the azimuth and elevation position offsets from the fitted Gaussian gives the full pointing information of each detector. To reduce the bias in the atmospheric filtering from the calibrator source signal, we repeat the above procedure with a 2^{nd} order polynomial, using the previously measured beam shape parameters to mask the source from filtering. We measure a mean beam FWHM of 58" for the array. The telescope pointing is measured every $1-2$ hours during an observing session by mapping a bright radio source or quasar. If the target appears offset by 10" or greater a pointing correction is applied.

We measure the flux calibration parameters from the same Mars scan. The ratio between the expected sky power per bandwidth, and the amplitude of the measured signal from the calibrator source gives the sky power to-ADC-count conversion. The expected sky power is the difference between the total source power and the power emitted from the CMB, adjusted by an integration factor which accounts for the radial size of the source compared to our Gaussian beams. Observations of Mars at 150 GHz are well in the Raleigh-Jeans region of the blackbody spectrum allowing a simple conversion from sky power to temperature using $P = 2 \times K_b \times Temp \times \Delta\nu$, where P is the sky power, K_b is Boltzmann's constant and $\Delta\nu$ is our observing bandwidth.

The atmospheric opacity will have an effect on the calibration of telescope observations taken at different elevations. We correct for atmospheric opacity using information from multiple skydips over the night. During a skydip, the telescope samples the airmass signal by scanning to a wide range of elevations along a constant azimuthal direction. The observed sky power is fit to the cosecant airmass signal, which ranges from 3 to 1 for elevations between 20° and 90°, and the same night's calibration scan data is used to convert to a temperature-per-airmass. The kelvin per airmass ratio for each observing day is calculated from the mean of the skydips, where the skydip ratio is the median channel ratio. We assume a sky temperature of $250K$ to convert the kelvin per airmass ratios to an opacity. Figure 4–6 shows each channel's change in signal as a function of airmass for a signal skydip, and the temperature-per-airmass ratios for each channel over all the skydips during an observation night. Any scan taken at an elevation equal to that of the calibration scan will not be affected by the opacity, but scans at different elevations are adjusted by a factor of (1−calibration airmass × opacity)/(1−scan airmass × opacity).

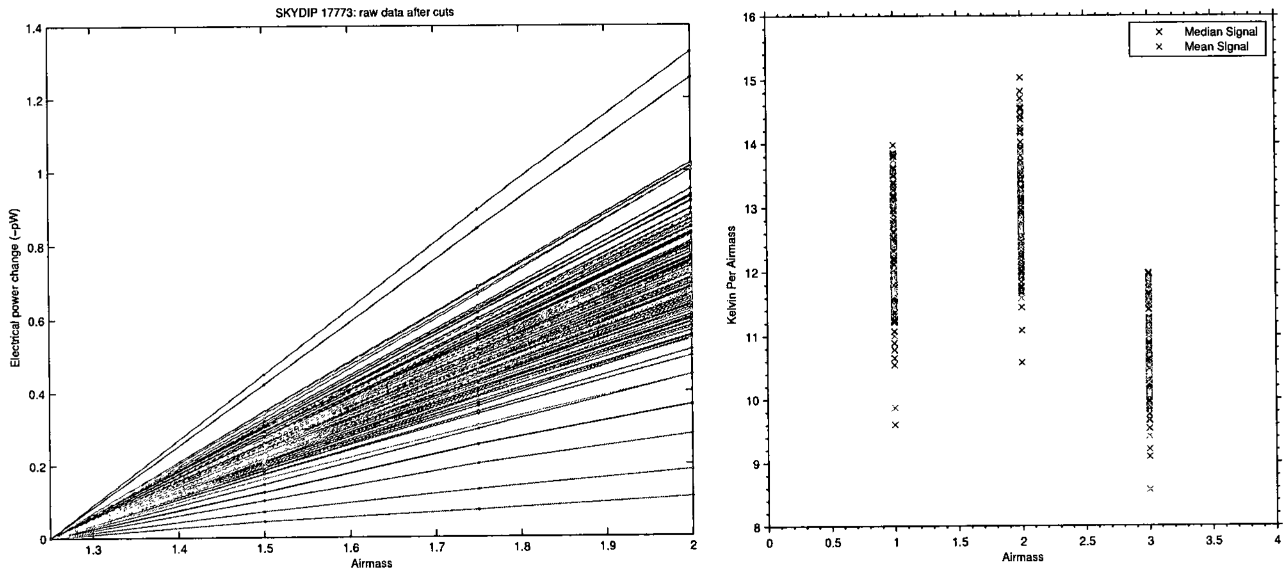

Figure 4–6: Opacity measurements from May 24^{th} 2008 skydips. Left: The change in electrical power across the detector, for a range of airmasses. Right: The airmass temperature measurements from individual channels for each skydip over the night.

During the May 2008 science observing run Mars would set below the minimum observing elevation of 30° early in the evening. This did not allow much time for a calibration scan after our daily detector tuning so we used a bootstrapped method of calibrating to gain more flexibility in our observing time-table. This consisted of doing a complete calibration scan of Mars and a secondary calibrator source both in one night. Assuming that the flux and radial profile of the secondary source remained constant, we could bootstrap off the Mars calibrations to find an effective secondary source temperature[2] and use either source as a calibrator for the remainder

[2] This is the temperature we would measure if the source had the same radial profile as our beam.

of the run. We chose to use RCW38 and IRAS12073-6233 as our secondary sources since they are both bright, stable HII regions.

These sources are both larger than our beam resolution. Due to the lack of information on their radial profiles at a fine angular resolution, we are unable to accurately measure any beam parameters other than amplitude. The remaining beam parameters are governed primarily by the optics of the telescope and since there has been no large change to the telescope or the instrument cabin environment, we use the previous Mars calibration beam size parameters for any bootstrapped calibration. This is acceptable if we know that the beam parameters do not change much over time. To check this, we look at beam parameters measured from four different Mars raster scans, each from a different observing run. Scan 5656 was chosen for the April 2007 observing run, scan 28940 from the August 2007 run, scan 52500 from the December run, and scan 17680 from the May 2008 observing run. Figure 4–7 shows that the measured FWHMs of the beams as a function of distance from the centre of the focal plane remain similar throughout each observing run. Focusing on the reference channel in figure 4–8, we can see that the x and y offsets are stable within 6 arcseconds and the FWHM are both stable within 3 arcsecs.

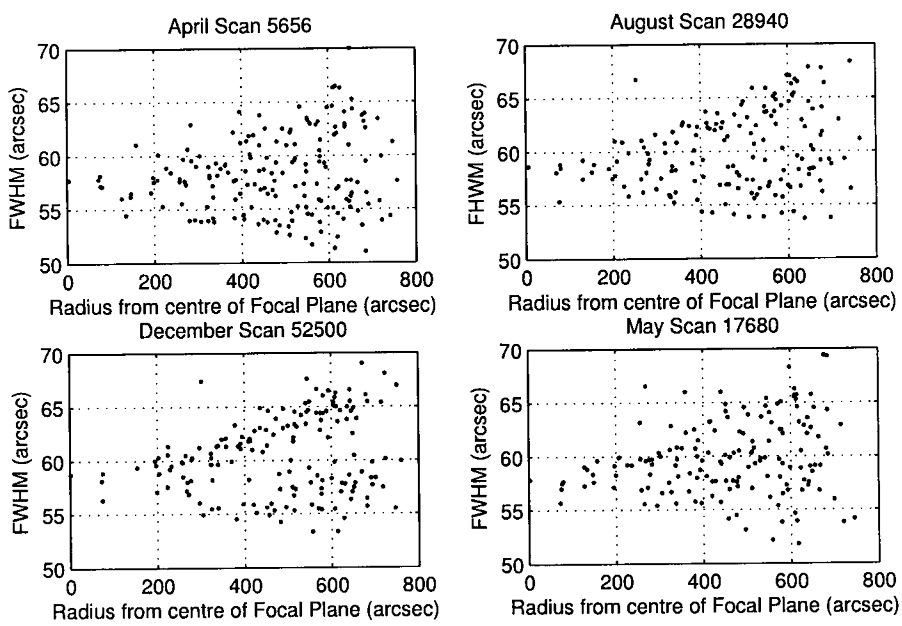

Figure 4–7: The measured FWHM of detector beams from each science observing run.

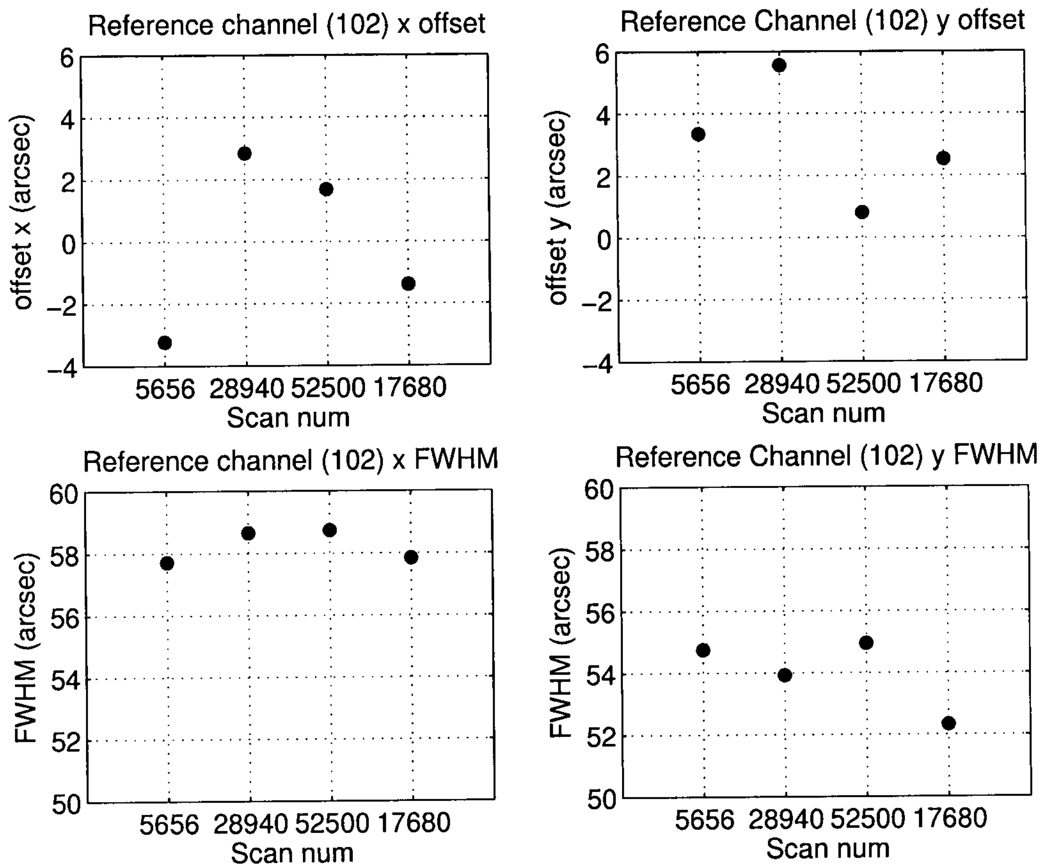

Figure 4–8: The measured FWHM for the reference channel from each science observing run.

The two secondary calibrator sources are both significantly dimmer than Mars, and have a non-Gaussian radial profile. The signals from these sources have amplitudes comparable in size to glitches, which appear randomly in the data. Proper processing must be applied to the timestreams to select the proper signal amplitude for the source temperature calculation and subsequent calibration conversions. We use the Mars beam parameter data, flagging optically dead and railed channels, then flagging a 3' region centred on the source coordinates. We then filter the timestream data by removing a second-order polynomial and a first-order spatial template, both ignoring any flagged data points. Any data outside the flagged region are then set to zero to reduce the probably of large amplitude glitches in the data. A Gaussian is fit to the timestream, centred on the maximum data point. The amplitude of the resulting Gaussian fit is set as the beam amplitude.

The non-Gaussian profile of the calibrator can affect the fit, so we've implemented a recursive fitting method which will calculate the χ^2 value of the Gaussian fit. If the χ^2 is above some threshold, the region to which the Gauss function is fit is reduced and a new fit is attempted. After ten iterations, if the χ^2 threshold is not reached, the signal amplitude is set to 'not a number' and no calibration conversions are calculated for this channel.

The bootstrapped calibration method uses the measured temperature of our secondary sources to calculate the sky power we would measure in our detectors. The ratio of this sky power to our beam amplitude gives the calibration conversions. We compare the bootstrapped calibrations to the direct Mars calibrations on a map of RCW38, measured on April 6^{th} 2007. The temperature of RCW38, measured on May 24^{th} 2008, is used to calibrate the map of RCW38 and the individual channel conversion factors are compared to the measured calibration conversion factors from a Mars raster scan taken on the same day. The bootstrapped calibration method introduces a 5% error on the direct Mars calibration. The channel-by-channel errors, along with a histogram of the relative differences from the Mars calibration is shown in figure 4–9

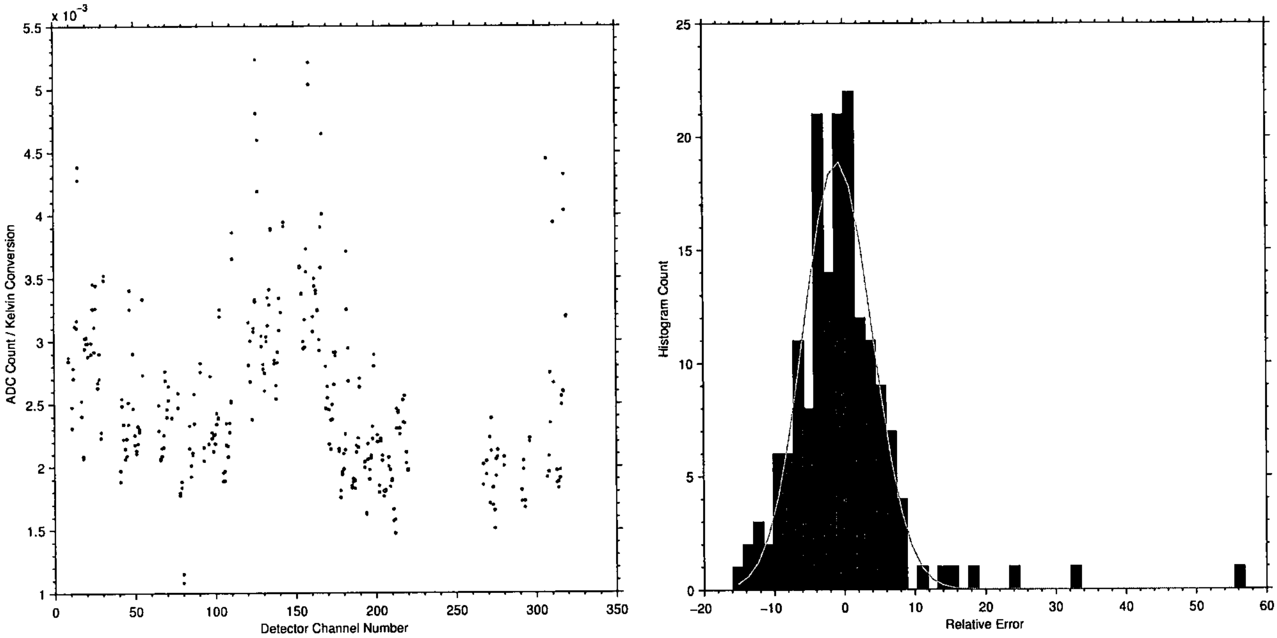

Figure 4–9: LEFT: The channel-by-channel conversion factors measured from Mars scan 5707 and bootstrapped using RCW38 scan 5683. RIGHT: The percentage difference between the Mars calibration and the bootstrapped RCW38 calibration shown on the left. The green line is the best-fit Gaussian with a sigma of 4.8. The effective temperature for RCW38 was measured using the Mars scan 17680 and the RCW38 scan 17687

The Mars flux at 150GHz and radial profile is obtained from the JCMT FLUXES program[3] which incorporates a thermal model for Mars developed by Wright [39] with an assigned 5% error. Recent WMAP observations of Mars find that the FLUXES program temperatures at 150GHz are over predicted by 10% [19] so we scale our temperatures temperatures down accordingly. Our measured Mars signal varies from day to day for reasons which are not well understood, but could be attributed to dust storms on the planet. We add an uncertainty of 3% to account for these variations. The uncertainty in our observing band centre introduces a 1.4% contribution to the total calibration uncertainty producing a final Mars calibration is 6%. The bootstrapping method has an additional 5% uncertainty resulting in a 7.8% total uncertainty for the bootstrapped calibrations.

[3] http://www.jach.hawaii.edu/jac-bin/planetflux.pl

4.4 Map Making

To produce a two-dimensional map of the CMB sky, each of the detectors needs pointing information to accompany its timestreams. The APEX telescope pointing data are interpolated to the data sampling frequency and applied to the reference detector channel. The pointing data for the remaining detectors are calculated from this reference channel and the beam offsets measured from the Mars calibration. The timestream can then be binned in angular sky coordinates to create a map. The individual channel maps are then coadded into a scan map, where each channel map is given a weighting based on the inverse of its timestream variance. Coaddition of the channel maps will not affect any correlated signal between the maps, such as the target cluster, but any uncorrelated noise remaining in the timestreams will decrease by a factor of $1/\sqrt{N}$. Scan maps can then be coadded together using a pixel-by-pixel minimum variance weighting to produce a high signal-to-noise map. Temperature profile models for galaxy clusters can then be fitted to the sky maps to measure the best fit values of cluster properties, such as central electron density and β value.

The resulting sky maps are our best representation of the CMB sky and a data set to which we can fit temperature and density profiles. However, the filtering applied for both these ends is not necessarily identical. In applying filters to subtract atmospheric signal and noise from our timestreams, we inevitably subtract cluster signal and degrade the cluster image in the map. If we can quantify the reduction in cluster signal, accurate model fitting can still be applied. We split our analysis at this point to both provide visual details of the cluster in our maps, and to make the best estimates of model parameters from our data.

For our maps, we use the telescope pointing data to mask the central region of our maps, thereby removing any cluster signal from the polynomial+secant and spatial template removal fitting algorithms. The masking prevents any influence of the cluster signal on the reduction. The polynomial+secants and spatial templates are then best fitted to the noise around the cluster. When removed from the whole dataset, including the cluster data, the the sky maps can show any extended emission and morphology of the cluster.

The source masked reductions has two notable flaws. The masking of the cluster also masks the noise on the cluster, which prevents the filters from fitting and removing the noise in that region. Also, it is difficult to quantify how the filters act on the source, making it difficult to produce a filter transfer function. We use a non-source masked data reduction for our model fitting analysis to both take advantage of the higher signal to noise of the cluster region, and to accurately quantify the filter transfer function.

CHAPTER 5
Analysis

The observations and data reduction described in chapter 4 produce a final map product. To make scientifically useful statements about individual clusters from their SZE map and to compare with observations at other wavelengths, we must select an appropriate cluster model. We use an isothermal β-model [5], generalized to fit clusters with ellipticity. Although a typical cluster's profile is expected to be more complex than a simple β-function, this model is common in the literature and allows for a direct comparison with previously determined values. We estimate the β-model parameters by simulating a number of β-model clusters, each with a different parameter set, and comparing their transfer-function-convolved simulated profile with the SZE data using a χ^2 statistic. These fits take into account the map noise and possible CMB primary anisotropies. A Markov-Chain Monte Carlo algorithm is used to sample the likelihood space and produce the likelihood distribution for the model parameters. Using the SZE derived β-model parameters and X-ray observations we can measure f_{gas} for the targeted cluster. Preliminary results of this analysis for two clusters are presented.

5.1 The Isothermal β Model

We model the ICM of our targeted clusters with an isothermal β-model. The subsequent f_{gas} analysis assumes that the cluster is both isothermal and in hydrostatic equilibrium. Both these assumptions are unphysical for some galaxy clusters. The Bullet cluster, for example, is a dynamical system of two colliding galaxy clusters in which the dark matter and galaxy components have been separated from the ICM medium. However, at the angular resolution and sensitivity of the APEX-SZ experiment, these assumptions are sufficient for analysis and comparison with other wavelength observations.

The three-dimensional β-model describes the electron density in the ICM as having a central maximum value which falls off radially with a power-law index. The form is shown in 5.1

$$n_e(r) = n_{eo}(1+\frac{r^2}{r_c^2})^{-3\beta/2} \tag{5.1}$$

where n_e is the electron density, n_{eo} is its central value, r_c is the radius at which the electron density has dropped to $2^{3\beta/2}$ its central value, or as it is more commonly known, the core radius.

The SZE temperature profile for this model is described by

$$\Delta T_{SZE} = \Delta T_o(1+\frac{\theta^2}{\theta_c^2})^{(1-3\beta)/2} \tag{5.2}$$

where ΔT_o is the central CMB temperature decrement, given by equation 1.4, and $\theta_c = r_c/D_A$. We have generalized the β model to account for ellipticity in clusters by setting $\theta = A+B$ where

$$A = cos(\Phi)(X-X_o) + sin(\Phi)(Y-Y_o) \tag{5.3}$$

$$B = \frac{-sin(\Phi)(X-X_o) + cos(\Phi)(Y-Y_o)}{\eta} \tag{5.4}$$

In these calculations, $(X-X_o)$ and $(Y-Y_o)$ are angular offsets from the central sky position, η is the axial ratio between the major and minor axes of the cluster, and Φ is the angle between the major axis and the RA direction.

If we now assume the ICM density has an oblate spheroidal symmetry, we can calculate the gas mass from integration of the gas density profile.

$$M_{gas} = 8\mu_e n_{eo} m_p D_A^3 \int_0^{r/D_A} (1+(\frac{X}{\theta_c})^2+(\frac{Y}{\eta\theta_c})^2+(\frac{Z}{\theta_c})^2)dXdYdZ \tag{5.5}$$

where m_p is the mass of the proton, n_{eo} is the central electron density, μ_e is the nucleon/electron ratio and the integral is taken over one octant of the spheroid. This equation reduces to M_{gas} for a spherical gas density in the limit $\eta = 1$.

The total mass can be calculated from the gas density distribution and X-ray data by solving the hydrostatic equilibrium equation

$$\rho_{total} = -\frac{kT_e}{4\pi G\mu m_p}\nabla^2 ln\rho_{gas} \tag{5.6}$$

where μ is the mean molecular weight of the ICM. By inserting the estimated β-model parameters and X-ray temperatures into equations 5.5 and 5.6, we can calculate the mass of the ICM, total cluster mass and gas mass fraction for the cluster. We integrate all radii out to r_{2500}, the radius at which the mean density of the cluster is 2500 times greater than the critical density of the universe. This truncates the β profile, which becomes unphysical at large radii. All calculations assume a ΛCDM cosmology with $\Omega_\Lambda = 0.73$, $\Omega_m = 0.27$, and $h = 0.7$.

5.2 Model Fitting

We fit the β-model to the central $7' \times 7'$ region of our sky map. The 7 model parameters we fit are given in table 5–1. We estimate our parameters by creating a number of simulated clusters with various β profiles and compare them with our sky map. For a direct comparison we need to quantify the effect our beam and filters have on these simulated clusters. We measure this effect using the transfer function of the filter set. The transfer function is measured by first creating noiseless timestreams for a simulated point source that has been convolved with our instrument beam. We then filter those timestreams using the sky map reduction filters for the cluster map [18] [35]. The resulting map is the transfer function. By convolving the simulated clusters with the transfer function, we produce the same result we would get by running the simulated cluster through the non-source flagged reduction pipeline, but at a small fraction of the time. Figure 5–1 shows an example of a simulated β-model cluster, a filter transfer function, and the result of a the convolution of the simulated cluster with the transfer function.

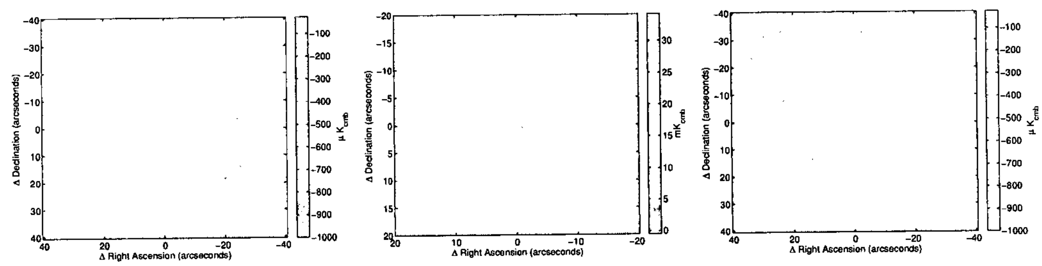

Figure 5–1: Left: A simulated β-model cluster. Middle: A transfer function resulting from sending a noiseless point source through the APEX-SZ pipeline. Right: The simulated cluster after a convolution with the transfer function.

To compare the simulated cluster to the sky map using a χ^2 statistic, we need a measure of the noise in the map. The noise term in the χ^2 is measured using jackknifes of the individual scan

Table 5–1: β-model parameters

Parameter	Description
X_o	The Right Ascension (RA) position of centroid
Y_o	The Declination (DEC) position of centroid
ΔT_o	The central temperature decrement
β	The model power-law index
θ_c	The core radius
η	The axial ratio between the major axis and minor axis
Φ	The orientation angle between major axis and RA axis

maps. A jackknife procedure consists of making two coadded maps, each consisting of half the individual scan maps. The jackknifed map is produced by subtracting one map from the other. This will remove any signal that is correlated between the maps, such as the galaxy cluster, but the uncorrelated noise in the maps will average down in the same manner as if we added the maps to produce the full coadded map.

Three issues must be addressed when estimating map noise using this technique. First, since our individual scan maps are typically taken over a period of days and under different atmospheric conditions, residual atmosphere may remain in some scan maps more than others and could bias our noise estimate from a single jackknife. Secondly, the maps are large enough to detect primary CMB anisotropies. This signal, common to all scan maps, would be removed during the jackknifes and erroneously neglected during the model fitting. Thirdly, to fully sample the noise covariance matrix using this method, we would need to generate an excessively large number of different jackknife maps.

To deal with the third issue, we make the assumptions that the noise is stationary in the map basis and the map coverage is uniform. With these assumptions, the noise-covariance matrix in the Fourier domain is a diagonal matrix with elements equal to the noise map power-spectral-density (PSD) [33]. We address the first issue by creating 500 jackknifes. Each of the jackknifed maps is created from randomly selecting the individual scans to be used in the two coadded maps. The final Fourier domain noise covariance matrix is calculated from the average of the resulting PSD's. The random jackknifing process will effectively remove the bias introduced by jackknifing scan maps with residual atmosphere.

To account for primary CMB anisotropy contributions to the covariance matrix, we generate a CMB realization using the WMAP5 best fit power spectrum. We convolve our primary CMB map with our transfer function to produce the effect of the beam smoothing and filter set, then we add it to the jackknife maps before their PSD's are calculated.

Our χ^2 statistic for the fit is

$$\chi^2 = (\widetilde{M} - \widetilde{\beta})^T \widetilde{C}^{-1} (\widetilde{M} - \widetilde{\beta}) \tag{5.7}$$

where $\widetilde{M}$ is the Fourier transform of the sky map, $\widetilde{\beta}$ is the Fourier transform of the filtered simulated β-model cluster, and $\widetilde{C}^{-1}$ is the inverse of the covariance matrix described above.

The χ^2 statistic is evaluated over the likelihood space, sampled using a Markov-Chain Monte Carlo method to be described in § 5.3. At each step in the likelihood space, the β-model parameters are used in equations 5.5 and 5.6 to calculate the ICM gas mass, total mass and gas mass fraction. The estimated model parameters, gas mass, total mass, f_{gas} values and their uncertainties are measured from the likelihood distributions.

5.3 Markov Chain Monte Carlo Likelihood Analysis

Multi-parameter model fits to the SZE maps of galaxy clusters using a brute-force likelihood method quickly become impractical as the number of parameters of interest increase. Our ellipsoidal beta model has seven parameters. Numerical integration of the likelihood space using a seven dimensional grid with just 10 points along each axis would require 10^7 calculations, taking about a month of CPU time on our computers. We use a Markov-Chain Monte Carlo (MCMC) method to intelligently sample the parameter space and reduce the computational time requirements for the likelihood fit.

An MCMC analysis method creates a random walk in the high dimensional parameter space, where the probability of taking each step depends only on the previous position. If an appropriate acceptance criterion is used for each step, then the sampled distribution will eventually converge toward the stationary likelihood distribution. The acceptance criteria we use is known as the Metropolis-Hastings algorithm. This algorithm starts with some parameter set Θ and corresponding likelihood $\mathcal{L} = e^{-\chi^2(\Theta)/2}$. A random step is made in parameter space generating a new parameter set, Θ' and the corresponding likelihood of the new parameter set, $\mathcal{L} = exp^{-\chi^2(\Theta')/2}$. The acceptance probability of this new step is given by [13]

$$\alpha(\Theta', \Theta) = min(1, e^{[-\chi^2(\Theta')+\chi^2(\Theta)]}) \tag{5.8}$$

Which states that if the likelihood of the new state is greater than the previous state, the new state is guaranteed to be accepted. If the likelihood of the new state is less than the likelihood of the previous state, the new state will be accepted with a probability equal to the ratio of the new likelihood state to the old likelihood state.

The MCMC chain described above will converge to the likelihood distribution after some number of steps. However, initially the MCMC chain will not have adequately sampled the parameter space, and the early samples could be heavily weighted by the local likelihood distribution rather than the global distribution. Unfortunately there is no 'smoking gun' test to indicate when the MCMC has appropriately sampled the likelihood distribution, but there are many methods for estimating its convergence. We have chosen to use the popular Gelman-Rubin statistic as an indication of convergence. The Gelman-Rubin statistic compares the variance within and between multiple chains to calculate an 'estimated potential scale reduction', $\hat{R}$, indicating how improved the convergence can become with further MCMC steps. Here the inter-chain variance, B, and the intra-chain variance, W, give an upper bound estimate of the variance $v\hat{a}r = \frac{n-1}{n}W + \frac{1}{n}B$ for each dimension in the parameter space. $\hat{R}$ is the ratio of this upper bound estimate to the lower bound estimate W.

$$\hat{R} = \frac{v\hat{a}r}{W} \tag{5.9}$$

An $\hat{R}$ value close to 1 will indicate convergence in the MCMC chains since the variations between the chains will nearly equal the variations within the chains [13]. Our implementation of the MCMC method uses only one chain, which we divide up into a number of equal sized chains for the Gelman Rubin convergence tests. We typically split our full MCMC chain into 3 sections, each 500 steps in length, to calculate the B and W values for each parameter. Once the $\hat{R}$ statistic has decreased below an upper threshold of 1.02 in every parameter dimension, the MCMC chain is considered to have converged.

Another consideration for MCMC chain convergence is the 'burn-in' period. This period occurs when the initial steps of the MCMC chain heavily depend on the local likelihood distribution and hence, the user-defined chain starting point. These steps are not considered fair samples of the distribution and are discarded. Our implementation discards the initial 0.5% of the chain to remove the burn-in period.

The practical rate at which convergence is reached will depend on the length scale of the likelihood space. To increase the rate of convergence, we estimate an initial step-size parameter in each dimension that is appropriate for the length scale of that model. For example, in our beta model fits we expect the positional offsets to be on the order of arcseconds, whereas the temperature values could vary on scales equal to the noise in the map. For the Bullet Cluster elliptical beta model fit, we set initial step size parameters for $X_o, Y_o, \Delta T_o, \beta, \theta_c, \eta, \Phi$ to be 3", 3", $50\mu K_{cmb}$, 10", 0.15, 0.05, and 10° respectively. The MCMC chain randomly chooses a step size in each dimension from a normal distribution centred on zero with σ equal to the step-size parameter.

After some number of steps, it may become evident that the initial step-size parameter is not the most efficient for the likelihood space. To speed up the convergence, we calculate a new step size parameter using the covariance from the first 1000 steps of the MCMC chain. Subsequent steps are made in the directions of the eigenvectors for the covariance matrix with a step size parameter equal to the corresponding eigenvalue. We apply this update early enough in the MCMC chain to prevent any disruption of the Markov-chain independent sampling property for final distribution.

5.4 Results

The full β-model analysis has been performed on both the Bullet Cluster and the cluster Abell 2204 (A2204). These are two of the many targeted clusters observed by the APEX-SZ experiment, and current work is being done to process the rest of the SZE data. Due to a strong degeneracy between the β parameter and the θ_c parameter in the β-model, we either set beta to a fixed value or apply a prior, derived from X-ray observations, to the β power law index. The cluster specific details are described below.

5.4.1 The Bullet Cluster

The cluster 1E0657-56, or the Bullet cluster as it is more commonly known, is an interesting dynamical system of two merging clusters at a redshift of $z = 0.296$. The collision is occurring in a plane perpendicular to the line of sight and, although the sub-structure of the collision can't be resolved with our beams, there is a visible elongation seen in its source flagged reduction map. The source flagged reduction map, along with a jackknifed map to indicate the level of map noise, is shown in figure 5–2. During our analysis we assume an electron temperature of $T_e = 13.9 \pm 0.7 keV$ measured by CHANDRA [14]. This temperature is in agreement with other X-ray observations. We apply a lopsided Gaussian prior to our β value, centred at $1.04^{+0.16}_{-0.10}$ to match ROSAT HRI X-ray measurements [28]. Although simulations have shown that typically SZE derived β values are larger than that from X-ray observations with a ratio $\beta_{SZE}/\beta_{X-ray} = 1.21 \pm 0.13$ [17], the uncertainties on our prior are large enough to account for the discrepancy. The results are shown in table 5–2 [1].

For the f_{gas} and cluster mass analysis we need values for μ_e, used in equation 5.5 and for μ, used in equation 5.6. For the Bullet cluster we assume the values $\mu_e = 1.16$ from OVRO/BIMA analysis [15] and $\mu = 0.62$ from REFLEX survey analysis [40]. Due to the ellipticity of the cluster, we assume an oblate spheroid The resulting f_{gas} of 0.140 ± 0.035, shown in table 5–4, is consistent with X-ray measurements.

[1] The uncertainties are quoted at the 68% confidence level. The uncertainty in ΔT_o includes a $60\mu K$ statisitical uncertainty and a $\pm 6\%$ flux calibration uncertainty. The uncertainties in the X_o and Y_o parameters include a ± 4" pointing uncertainty

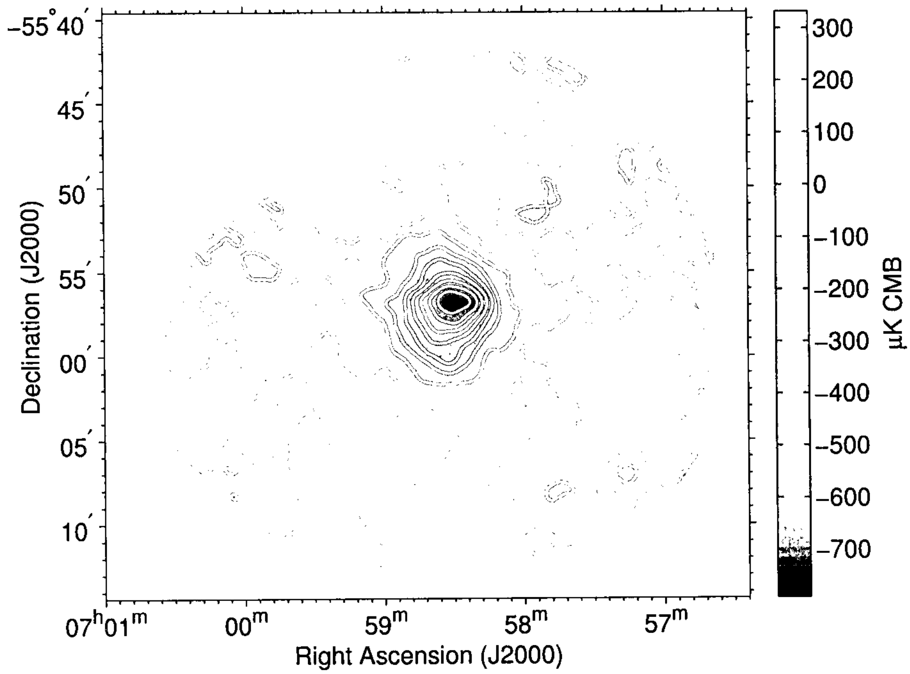

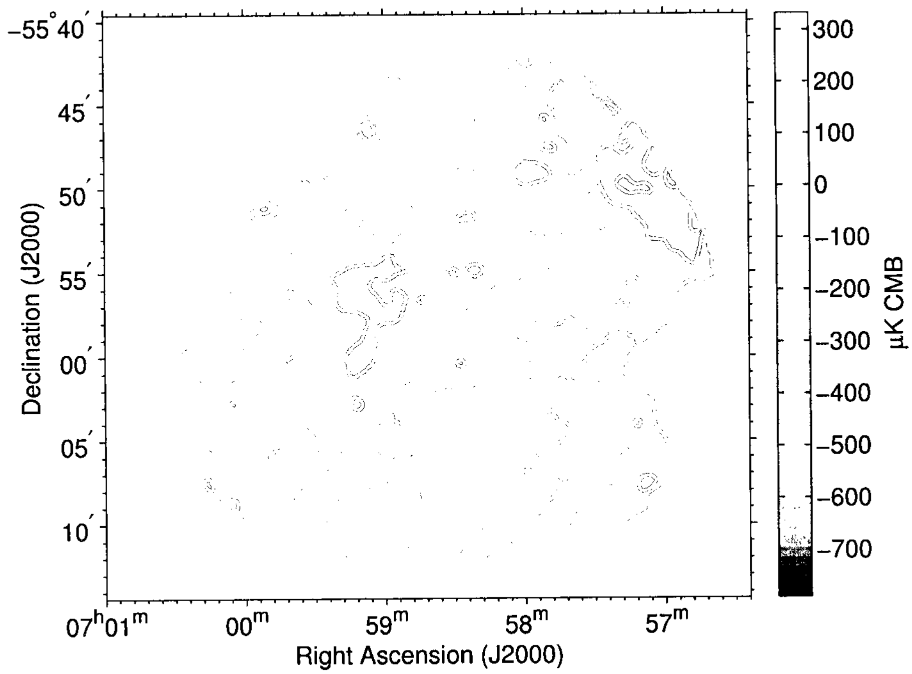

Figure 5–2: Top: The Bullet Cluster map from a source-flagged data reduction. The source has been masked out to a radius of 4.75' during the filter fitting steps. Bottom: A jackknifed map from individual Bullet scan maps to give a visual representation of the noise levels in the Bullet map(top). Both maps have been smoothed with a 1' FWHM Gaussian, on top of the instrument beam and reduction filter, to reduce noise on scales smaller than the beam. The resolution of both maps is 85". Contour lines are separated by $100\mu K_{cmb}$.

Table 5–2: β-model Parameter Estimates for the Bullet Cluster

Parameter	Value	Uncertainty
X_o	$06^h58^m31.41^s(J2000)$	± 7.5"
Y_o	$-55°56'57.9"(J2000)$	± 8.7"
ΔT_o	$-880\mu K_{cmb}$	$\pm 80\mu K_{cmb}$
β	1.16	± 0.12
θ_c	144"	± 19"
η	0.881	± 0.086
Φ	$-70°$	$\pm 20°$

5.4.2 A2204

The cluster A2204, shown in figure 5–3, is at a redshift of $z = 0.152$. It has previously been observed in X-ray with CHANDRA and its SZE signal has been observed using BIMA. We use the CHANDRA X-ray temperature, $T_e = 11.23^{+0.85}_{-0.72}$ for the analysis. Previous analysis of the combined BIMA and CHANDRA data has measured β assuming either an isothermal β-model with the central 100kpc region of the cluster removed during the fit, or a non-isothermal double-β profile which accounts for temperature variations across the gas. Both models find β values ~ 0.6 with uncertainties$< 10\%$ [3] [23]. In these analyses, the β parameter is largely driven by the X-ray data. A third model used assumes an isothermal β-model, with β fixed to 0.7, and fits using only the SZE data. In our analysis, we adopt the fixed $\beta = 0.7$ value assumed in previous SZE-only analysis [23]. This β value is consistent with the $\beta_{SZE}/\beta_{X-ray}$ factor. The results are shown in table 5–3 [2]

For the f_{gas} and cluster mass analysis we again assume the values $\mu_e = 1.16$ and $\mu = 0.62$. We measure an f_{gas} of 0.058 ± 0.035, shown in table 5–4. This gas fraction is inconsistent with the gas mass fraction measured by the BIMA SZE-only analysis. However, both X-ray and SZE analysis show large variations in the gas mass fraction, depending on the assumed model and

[2] The uncertainties are quoted at the 68% confidence level. The uncertainty in ΔT_o includes a $102\mu K$ statisitical uncertainty and a $\pm 7.8\%$ flux calibration uncertainty. The uncertainties in the X_o and Y_o parameters include a ± 4" pointing uncertainty

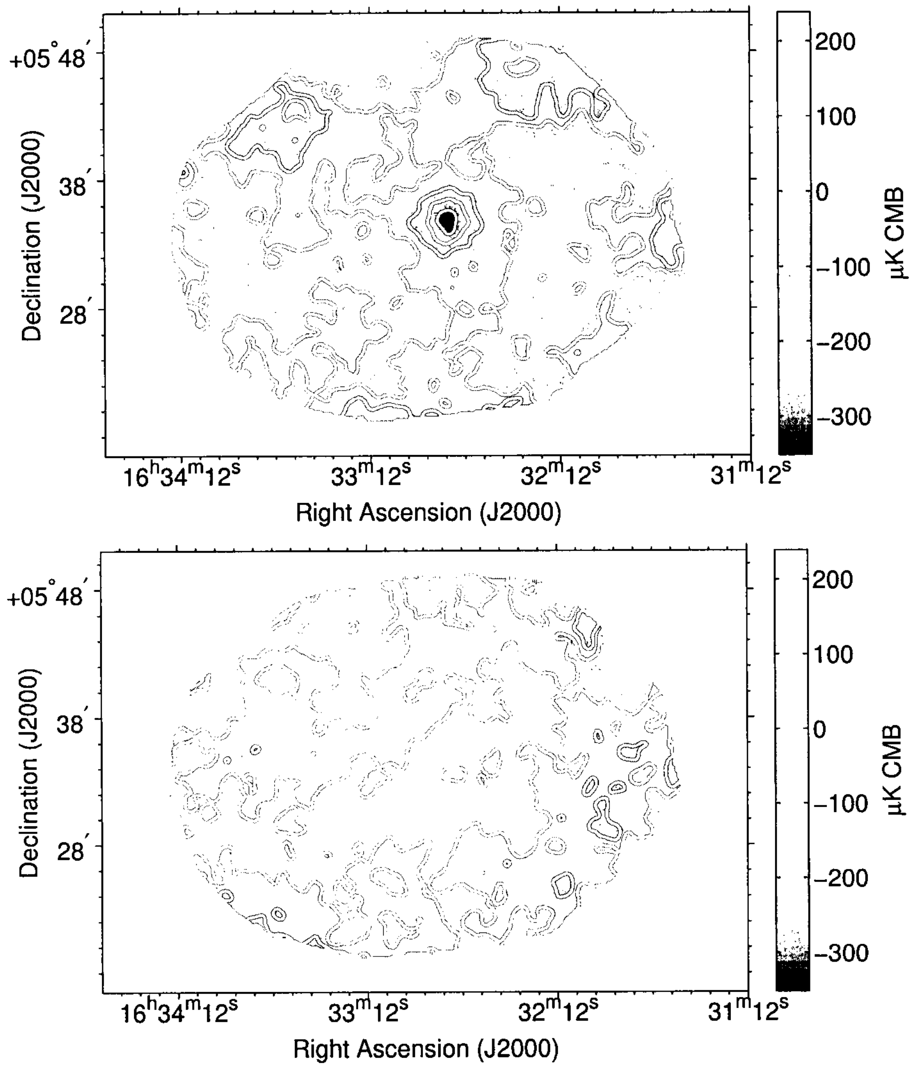

Figure 5–3: Top: The A2204 cluster map using the source-flagged data reduction. The source has been masked out to a radius of 3' during filter fitting steps. Bottom: A jackknifed map from individual A2204 scan maps. This map gives a visual representation of the noise levels in the A2204 map(top). Both maps have been smoothed with a 1' FWHM Gaussian, on top of the instrument beam and reduction filter, to reduce noise on scales smaller than the beam. The resolution of both maps is 85". Contour lines are separated by $100\mu K_{cmb}$.

data set combinations. The combined X-ray and SZE analysis with an assumed isothermal β-model and 100kpc central cut measures an $f_{gas} = 0.086^{+0.010}_{-0.011}$, which is on the lower side of their sample mean value of $0.116^{0.009}_{-0.026}$. SZE-only analysis measures an $f_{gas} = 0.180^{+0.069}_{-0.051}$, which is on the higher side of their sample mean value of 0.120 ± 0.009. Both the sample mean values of the previous analysis are consistent with CHANDRA results [23]. A comparison of our derived β-model parameters with that from the X-ray and SZE analysis shows that our θ_c values are in agreement when the X-ray observations constrain parameter fitting. However, the SZE-only analyses estimates a θ_c which differs from ours by a factor of 2. Our f_{gas}, the previously derived f_{gas} from combined X-ray and SZE measurements, and the previously determined SZE-only f_{gas} remain inconsistent with each other. Interestingly ROSAT observations of A2204 have produced β-model parameters and f_g estimates in agreement with ours [12]. The origin of the scatter in β-model parameters between different experiments is unknown. The extreme sensitivity to the assumed gas density model could indicate that the cluster is not accurately described by an isothermal β model in hydrostatic equilibrium. A detailed analysis including weak-lensing data, and a more sophisticated density model, is required to increase confidence on the derived f_{gas} for this cluster.

Table 5–3: β-model Parameter Estimates for the Cluster A2204

Parameter	Value	Uncertainty
X_o	$16^h32^m47.43^s(J2000)$	±12.4"
Y_o	5°34′48.8"$(J2000)$	±14.8"
ΔT_o	-656μK_{cmb}	±153μK_{cmb}
θ_c	43.3"	±23"
η	0.900	±0.196
Φ	47°	±76°

5.5 Cosmological Measurements using Cluster Gas Mass Fractions

The β-model parameter estimates for the Bullet cluster and A2204 detail the gas distribution in the ICM. Combining this model with the electron temperature, typically measured from X-ray observations, allows a measurement of the gas mass fraction of the cluster f_{gas}. The Bullet and

A2204 gas mass fractions are shown in table 5–4 [3]. A fraction of the baryonic content in a cluster will be contained in the galaxies. However, assuming that this fraction remains fixed, we can relate f_{gas} to the cosmic baryon fraction $f_{gas}(1+0.12) = \frac{\Omega_B}{\Omega_M}$ [37]. Using the Bullet f_{gas} and an $\Omega_B = 0.0456 \pm 0.0015$ [20] measured from the five-year WMAP results combined with data from Baryon Acoustic Oscillations(BAO) in the distributions of galaxies, and type Ia supernova surveys, we measure $\Omega_M = 0.326 \pm 0.082$.

Our result is in agreement with the current value of Ω_M, however there are a few sources of error in the measurement. First, recent simulations of galaxy clusters have shown that the cluster baryon fraction in galaxies may fluctuate depending on the gravitational heating, radiative cooling, and stellar formation processes within the cluster [11]. With tight constraints already placed on $\frac{\Omega_B}{\Omega_M}$, recent work has gone into using the SZE derived gas mass fractions to measure the ratio of the cluster gas mass fraction to the cosmic baryon fraction, $\eta_{gas} \equiv \frac{f_{gas}}{\Omega_B/\Omega_M}$ [23]. Secondly, the determination of the gas mass fraction from our SZE maps, originally depended on the assumed cluster model, hydrostatic equilibrium condition, and cosmology. A detailed analysis combining SZE gas mass data with the weak lensing derived total mass of the cluster would allow a gas mass fraction measurement independent of the cluster model and hydrostatic equilibrium assumptions [4].

Table 5–4: Cluster Mass Properties

Cluster	r_{int}(')	r_{int}(Mpc)	Gas Mass ($10^{14} M_\odot$)	Total Mass ($10^{14} M_\odot$)	f_{gas}
Bullet	2.82	0.752	1.07 ± 0.15	7.76 ± 1.24	0.140 ± 0.035
A2204	4.48	0.714	0.354 ± 0.035	5.90 ± 0.43	0.058 ± 0.035

[3] The integration radius is given as both an angle on the sky and as a physical radius.

CHAPTER 6
Conclusions

The interaction of CMB photons with the hot intergalactic gas in galaxy clusters produces the unique SZE signal. Measurements of the SZE provide details about the intracluster gas properties, which can then be used for cosmological measurements. The APEX-SZ experiment is a project dedicated to the measurement of cluster SZE signals. Mounted on the APEX telescope, the APEX-SZ instrument uses a large array of frequency domain multiplexed transition-edge sensor bolometers to achieve extremely sensitive measurements of the sky signal at 150GHz. APEX-SZ is the first experiment to use such an array to produce scientific results. A custom data analysis pipeline has been developed for the reduction and processing of the bolometer data. The final product is a CMB sky map with temperature decrements indicating targeted clusters. This thesis presents the CMB maps and data analysis of two known clusters; the Bullet cluster and A2204. We have used a Markov-Chain Monte Carlo algorithm to fit a multi-parameter isothermal β model to the data. Assuming hydrostatic equilibrium, we have calculated the total mass of the cluster from the SZE derived β model and X-ray electron temperature measurements. For the Bullet cluster, we measure $f_{gas} = 0.140 \pm 0.035$, and for A2204 we measure $f_{gas} = 0.058 \pm 0.035$. The Bullet gas mass fraction is consistent with previous X-ray and SZE observations, however the A2204 gas mass fraction varies from previous measurements and requires a more detailed analysis.

The preliminary gas mass fraction calculations presented in this thesis are a first step and ultimately a small demonstration of the potential cosmology achievable with the APEX-SZ experiment and the SZE. Combined analysis using X-ray, weak lensing, and SZE data will provide detailed information on the thermal structure of ICMs.The results of such an analysis will test the basic assumptions of cluster physics, such as hydrostatic equilibrium. In merging clusters especially, a study of the ICM will enable a deeper understanding of all the cluster components including its dark matter. The general SZE properties observed in individual targeted cluster measurements will also improve the constraints on SZE signal scaling relations. Understanding the scaling relations, such as the integrated SZE signal - cluster mass relation will improve the strategies and analysis of upcoming large-scale SZE sky surveys. These surveys will discover and catalogue many new galaxy clusters over a range of redshifts, providing information on the evolution of cluster abundance and cosmic energy densities.

Since its initial engineering run in December 2005, the APEX-SZ experiment has completed 5 separate observing campaigns, cumulating several weeks of cluster observations. 13 known clusters have been observed during these campaigns. The APEX-SZ will provide an increased SZE cluster catalogue when combined with the South Pole Telescope, which observes a separate area of sky. A bolometer array upgrade is planned for the spring of 2009 providing increased sensitivity and bolometer yield. This improved array will be used for the planned observing campaigns in April 2009, December 2009, and possible observations thereafter.

Aside from the observational results, the APEX-SZ experiment has provided the necessary technological background for new CMB experiments. The frequency domain multiplexing of TES bolometers is a novel design that easily lends itself to larger and larger detector arrays, such as the South Pole Telescope and the upcoming EBEX experiment. As the technology continues to develop, more detectors will be read out through a SQUID amplifier, reducing the wiring complexity and cost of cryogenic experiments. Again, the APEX-SZ experiment has provided the first step in the current direction of CMB experiments aimed at a greater cosmological understanding of the universe.

References

[1] C. L. Bennett, A. Kogut, G. Hinshaw, A. J. Banday, E. L. Wright, K. M. Gorski, D. T. Wilkinson, R. Weiss, G. F. Smoot, S. S. Meyer, J. C. Mather, P. Lubin, K. Loewenstein, C. Lineweaver, P. Keegstra, E. Kaita, P. D. Jackson, and E. S. Cheng. Cosmic temperature fluctuations from two years of COBE differential microwave radiometers observations. *Astrophysical Journal*, 436:423–442, December 1994.

[2] M. Birkinshaw. The Sunyaev-Zel'dovich effect. *Physics Reports*, 310:97–195, March 1999.

[3] M. Bonamente, M. K. Joy, S. J. LaRoque, J. E. Carlstrom, E. D. Reese, and K. S. Dawson. Determination of the Cosmic Distance Scale from Sunyaev-Zel'dovich Effect and Chandra X-Ray Measurements of High-Redshift Galaxy Clusters. *Astrophysical Journal*, 647:25–54, August 2006.

[4] J. E. Carlstrom, G. P. Holder, and E. D. Reese. Cosmology with the Sunyaev-Zel'dovich Effect. *Annual Review of Astronomy and Astrophysics*, 40:643–680, 2002.

[5] A. Cavaliere and R. Fusco-Femiano. The Distribution of Hot Gas in Clusters of Galaxies. *Astronomy and Astrophysics*, 70:677–+, November 1978.

[6] Chase, S. *Three-Stage Sub-Kelvin ^3He Cooler.* Chase Research Cryogenics Ltd, 2006.

[7] D. Clowe, M. Bradač, A. H. Gonzalez, M. Markevitch, S. W. Randall, C. Jones, and D. Zaritsky. A Direct Empirical Proof of the Existence of Dark Matter. *Astrophysical Journal Letters*, 648:L109–L113, September 2006.

[8] M. Dobbs, N. W. Halverson, P. A. R. Ade, K. Basu, A. Beelen, F. Bertoldi, C. Cohalan, H. M. Cho, R. Güsten, W. L. Holzapfel, Z. Kermish, R. Kneissl, A. Kovács, E. Kreysa, T. M. Lanting, A. T. Lee, M. Lueker, J. Mehl, K. M. Menten, D. Muders, M. Nord, T. Plagge, P. L. Richards, P. Schilke, D. Schwan, H. Spieler, A. Weiss, and M. White. APEX-SZ first light and instrument status. *New Astronomy Review*, 50:960–968, December 2006.

[9] V. R. Eke, J. F. Navarro, and C. S. Frenk. The Evolution of X-Ray Clusters in a Low-Density Universe. *Astrophysical Journal*, 503:569–+, August 1998.

[10] S. Ettori. Are we missing baryons in galaxy clusters? *Monthly Notices of the Royal Astronomical Society*, 344:L13–L16, September 2003.

[11] S. Ettori, K. Dolag, S. Borgani, and G. Murante. The baryon fraction in hydrodynamical simulations of galaxy clusters. *Monthly Notices of the Royal Astronomical Society*, 365:1021–1030, January 2006.

[12] S. Ettori and A. C. Fabian. ROSAT PSPC observations of 36 high-luminosity clusters of galaxies: constraints on the gas fraction. *Monthly Notices of the Royal Astronomical Society*, 305:834–848, May 1999.

[13] Gilks, W. R. and Richardson, S. and Spiegelhalter, D. J., editor. *Markov Chain Monte Carlo in Practice.* Chapman & Hall/CRC, 1996.

[14] F. Govoni, M. Markevitch, A. Vikhlinin, L. VanSpeybroeck, L. Feretti, and G. Giovannini. Chandra Temperature Maps for Galaxy Clusters with Radio Halos. *Astrophysical Journal*, 605:695–708, April 2004.

[15] L. Grego, J. E. Carlstrom, E. D. Reese, G. P. Holder, W. L. Holzapfel, M. K. Joy, J. J. Mohr, and S. Patel. Galaxy Cluster Gas Mass Fractions from Sunyaev-Zeldovich Effect Measurements: Constraints on Ω_M. *Astrophysical Journal*, 552:2–14, May 2001.

[16] R. Güsten, L. Å. Nyman, P. Schilke, K. Menten, C. Cesarsky, and R. Booth. The Atacama Pathfinder EXperiment (APEX) - a new submillimeter facility for southern skies -. *Astronomy and Astrophysics*, 454:L13–L16, August 2006.

[17] E. J. Hallman, J. O. Burns, P. M. Motl, and M. L. Norman. The β-Model Problem: The Incompatibility of X-Ray and Sunyaev-Zeldovich Effect Model Fitting for Galaxy Clusters. *Astrophysical Journal*, 665:911–920, August 2007.

[18] N. W. Halverson, T. Lanting, P. A. R. Ade, K. Basu, A. N. Bender, B. A. Benson, F. Bertoldi, H. . Cho, G. Chon, J. Clarke, M. Dobbs, D. Ferrusca, R. Guesten, W. L. Holzapfel, A. Kovacs, J. Kennedy, Z. Kermish, R. Kneissl, A. T. Lee, M. Lueker, J. Mehl, K. M. Menten, D. Muders, M. Nord, F. Pacaud, T. Plagge, C. Reichardt, P. L. Richards, R. Schaaf, P. Schilke, F. Schuller, D. Schwan, H. Spieler, C. Tucker, A. Weiss, and O. Zahn. Sunyaev-Zel'dovich Effect Observations of the Bullet Cluster (1E 0657-56) with APEX-SZ. *ArXiv e-prints*, July 2008.

[19] R. S. Hill, J. L. Weiland, N. Odegard, E. Wollack, G. Hinshaw, D. Larson, C. L. Bennett, M. Halpern, L. Page, J. Dunkley, B. Gold, N. Jarosik, A. Kogut, M. Limon, M. R. Nolta, D. N. Spergel, G. S. Tucker, and E. L. Wright. Five-Year Wilkinson Microwave Anisotropy Probe (WMAP)Observations: Beam Maps and Window Functions. *ArXiv e-prints*, March 2008.

[20] G. Hinshaw, J. L. Weiland, R. S. Hill, N. Odegard, D. Larson, C. L. Bennett, J. Dunkley, B. Gold, M. R. Greason, N. Jarosik, E. Komatsu, M. R. Nolta, L. Page, D. N. Spergel, E. Wollack, M. Halpern, A. Kogut, M. Limon, S. S. Meyer, G. S. Tucker, and E. L. Wright. Five-Year Wilkinson Microwave Anisotropy Probe (WMAP) Observations: Data Processing, Sky Maps, and Basic Results. *ArXiv e-prints*, March 2008.

[21] Josephson, B. D. Possible new effects in superconductive tunneling. *Physics Letters*, 1:251, 1962.

[22] Lanting, T. M. *Multiplexed Readout of Superconducting Bolometers for Cosmological Observations.* PhD thesis, University of California, Berkeley, 2006.

[23] S. J. LaRoque, M. Bonamente, J. E. Carlstrom, M. K. Joy, D. Nagai, E. D. Reese, and K. S. Dawson. X-Ray and Sunyaev-Zel'dovich Effect Measurements of the Gas Mass Fraction in Galaxy Clusters. *Astrophysical Journal*, 652:917–936, December 2006.

[24] O. P. Lay and N. W. Halverson. The Impact of Atmospheric Fluctuations on Degree-Scale Imaging of the Cosmic Microwave Background. *Astrophysical Journal*, 543:787–798, November 2000.

[25] Lee, A. and Richards, P. L. and Nam, S. and Cabrera, B. andIrwin K. A superconducting bolometer with strong electrothermal feedback. *Applied Physics Letters*, 69:1801, 1996.

[26] J. C. Mather, E. S. Cheng, D. A. Cottingham, R. E. Eplee, Jr., D. J. Fixsen, T. Hewagama, R. B. Isaacman, K. A. Jensen, S. S. Meyer, P. D. Noerdlinger, S. M. Read, L. P. Rosen, R. A. Shafer, E. L. Wright, C. L. Bennett, N. W. Boggess, M. G. Hauser, T. Kelsall, S. H. Moseley, Jr., R. F. Silverberg, G. F. Smoot, R. Weiss, and D. T. Wilkinson. Measurement of the cosmic microwave background spectrum by the COBE FIRAS instrument. *Astrophysical Journal*, 420:439–444, January 1994.

[27] J. Mehl, P. A. R. Ade, K. Basu, D. Becker, A. Bender, F. Bertoldi, H. M. Cho, M. Dobbs, N. W. Halverson, W. L. Holzapfel, R. Gusten, J. Kennedy, R. Kneissl, E. Kreysa, T. M. Lanting, A. T. Lee, M. Lueker, K. M. Menten, D. Muders, M. Nord, F. Pacaud, T. Plagge, P. L. Richards, P. Schilke, D. Schwan, H. Spieler, A. Weiss, and M. White. TES Bolometer Array for the APEX-SZ Camera. *Journal of Low Temperature Physics*, 151:697–702, May 2008.

[28] N. Ota and K. Mitsuda. A uniform X-ray analysis of 79 distant galaxy clusters with ROSAT and ASCA. *Astronomy and Astrophysics*, 428:757–779, December 2004.

[29] A. A. Penzias and R. W. Wilson. A Measurement of Excess Antenna Temperature at 4080 Mc/s. *Astrophysical Journal*, 142:419–421, July 1965.

[30] M.W. Pospieszalski. Millimeter-wave, cyrogenically-coolable amplifiers using all-nas/galnas/lnp hemts. *Microwave Symposium Digest*, 2:515, 1993.

[31] D. Rapetti, S. W. Allen, and A. Mantz. The prospects for constraining dark energy with future X-ray cluster gas mass fraction measurements. *Monthly Notices of the Royal Astronomical Society*, 388:1265–1278, August 2008.

[32] Richards, P. L. Bolometers for infrared and millimeter waves. *Jounal of Applied Physics*, 76:1, 1994.

[33] Sayers, J. *A search for Cosmic Microwave Background Anisotropies on Arcminute Scales.* PhD thesis, California Institute of Technology, 2004.

[34] D. Schwan, F. Bertoldi, S. Cho, M. Dobbs, R. Guesten, N. W. Halverson, W. L. Holzapfel, E. Kreysa, T. M. Lanting, A. T. Lee, M. Lueker, J. Mehl, K. Menten, D. Muders, M. Myers, T. Plagge, A. Raccanelli, P. Schilke, P. L. Richards, H. Spieler, and M. White. APEX-SZ a Sunyaev-Zel'dovich galaxy cluster survey. *New Astronomy Review*, 47:933–937, December 2003.

[35] K. S. Scott, J. E. Austermann, T. A. Perera, G. W. Wilson, I. Aretxaga, J. J. Bock, D. H. Hughes, Y. Kang, S. Kim, P. D. Mauskopf, D. B. Sanders, N. Scoville, and M. S. Yun. AzTEC millimetre survey of COSMOS field (Scott+, 2008). *VizieR Online Data Catalog*, 738:52225–+, September 2008.

[36] G. M. Voit. Tracing cosmic evolution with clusters of galaxies. *Reviews of Modern Physics*, 77:207–258, April 2005.

[37] S. D. M. White, J. F. Navarro, A. E. Evrard, and C. S. Frenk. The Baryon Content of Galaxy Clusters - a Challenge to Cosmological Orthodoxy. *Nature*, 366:429–+, December 1993.

[38] White, G. K. *Experimental Techniques in Low Temperature Physics.* Oxford University Press, 1968.

[39] E. L. Wright. Recalibration of the far-infrared brightness temperatures of the planets. *Astrophysical Journal*, 210:250–253, November 1976.

[40] Y.-Y. Zhang, A. Finoguenov, H. Böhringer, Y. Ikebe, K. Matsushita, and P. Schuecker. Temperature gradients in XMM-Newton observed REFLEX-DXL galaxy clusters at z 0.3. *Astronomy and Astrophysics*, 413:49–63, January 2004.